Study on Permeability Anisotropy of Sedimentary Rocks during Progressive Deformation under True Triaxial Stresses

February 2016

Minoru SATO

Study on Permeability Anisotropy of Sedimentary Rocks during Progressive Deformation under True Triaxial Stresses

A Dissertation Submitted to

the Graduate School of Life and Environmental Sciences,

the University of Tsukuba

in Partial Fulfillment of the Requirements

for the Degree of Doctor of Philosophy in Science

（Doctoral Program in Integrative Environmental Sciences）

Minoru SATO

Abstract

Study of underground fluid migration in sedimentary rocks is important for understanding deformation and seismogenic zone processes in accretionary prisms. It is also important for reservoir engineering such as evaluating water shielding structure for oil extraction, carbon capture and storage, and high-level radioactive waste disposal. In particular, underground fluid migration needs to be examined in terms of permeability, and its evaluation needs to take faulting into account, because faulting can change the geological structure and permeability of the underground environment. Computer simulations are generally used in estimating underground fluid migration; however, it is important to input appropriate hydraulic constants such as hydraulic conductivity and specific storage. Hence, the reliability of groundwater flow analysis depends on the accuracy of acquired hydraulic constants of the considered underground environment. There are some difficulties associated with acquiring data from in-situ measurements for deep underground or below the seafloor because of the requirement for drilling technology and the associated time and cost constraints. Therefore, it is crucial to measure physical parameters such as strength and hydraulic constants of rocks in laboratory experiments, assuming an underground stress state.

The stress states in an arbitrary underground depth at a static condition are basically calculated from overburden stress of rock and fluid column at the depth and assuming Poisson ratio of the rock. A number of studies have addressed a conventional triaxial compression test, in which a cylindrical core specimen is loaded axially to failure at constant confining pressure, to understand mechanical behavior of the rocks under uniaxial compressional or uniaxial extensional stresses ($\sigma_1 > \sigma_2 = \sigma_3$ or $\sigma_1 = \sigma_2 > \sigma_3$). The characteristics of rock strength, deformation and failure mainly originate from the conventional compression test. However, the rocks in nature undergo more complicated stresses: in the subduction zones as an example, the stress state is extremely complicated by lateral tectonic compression. Thus, a true triaxial test apparatus is required to simulate the general stress state ($\sigma_1 \geqq \sigma_2 \geqq \sigma_3$). Previous studies

using true triaxial test apparatus have revealed that σ_2 has a large control on the mechanical behavior, micro-crack distribution and strength of fractures that developed in the rock specimens. It is also expected that permeability depends on the triaxial stress conditions and that it must differ according to the orientation of the stresses; however, previous studies only measured the permeability in one direction parallel to the uniaxial compressional or extensional stresses. The purpose of this study is to evaluate the permeability anisotropy under the general stress state conditions. Experiments were conducted in which the permeability was measured in the σ_1 and σ_2 directions during differential loading with fixed σ_3 conditions.

Three conclusions can be drawn from the experiment results: 1) Hydraulic conductivity of both the σ_1 and σ_2 direction decreased with increasing stresses. 2) In the specimen after brittle deformation, the decrease of hydraulic conductivity in the σ_1 direction (across the fault) was larger than that of the σ_2 direction (parallel to the fault) under relatively high σ_2 conditions. Scanning electron microscopy showed the development of fault gouge in the specimen after experiments. The fine-grained fault gouge inhibited the fluid flow in the σ_1 direction by working as a sealing. 3) During ductile deformation of the specimens, hydraulic conductivity also decreased with increasing stress; however, permeability anisotropy was not observed after the failure.

This study developed new laboratory apparatus for the permeability measurement under arbitrary and changing natural stress states and method to unravel complicated hydrologic deformation processes. This study suggests that permeability anisotropy will be developed in sedimentary rocks due to formation of fault gouge under true triaxial test conditions.

Contents

List of Figures

List of Tables

1. Introduction

Study of underground fluid migration is important for understanding seismogenic zone processes of sedimentary rocks in accretionary prisms, such as how thermal expansion of fluid accelerates or terminates earthquake faulting, and influence of permeability structures on it. It is also important for reservoir engineering such as evaluating water shielding structure for oil extraction, Carbon Capture and Storage (CCS) and high-level radioactive waste disposal. In particular, subsurface fluid migration needs to be examined in terms of permeability, and its evaluation needs to take faulting into account, because faulting can change the geological structure and permeability of the subsurface environment.

In general, three mutually perpendicular principal stresses are addressed to describe a state of stress: the largest principal stress is referred to the maximum principal stress and represented by σ_1, the intermediate principal stress by σ_2 and the minimum principal stress by σ_3. Stress state at static underground conditions can be basically calculated using overburden pressure from rock and fluid columns. In accretionary prisms in the subduction zone, however, the stress state is extremely complicated by lateral tectonic compression (Ogawa et al, 1996) and a stair case geometry. In accretionary prism sediments, distribution of fractures, fault gouge and/or cataclasite may affect the permeability anisotropy. The direction of fluid flow in rocks depends on the hydraulic gradient and the permeability anisotropy of rocks (Farrell et al. 2014). For example, Sibson et al. (1975) showed the schematic diagram of fluid flow toward σ2 in the strike-slip stress regime with pressure relief after shallow earthquake (Fig. 1.1). The rapid relief of shear stress which accompanies earthquake faulting allows the cracks within the deformation zone to relax, and the fluids they contain must be flowed upwards. Ogawa et al. (1996) proposed that *en echelon Calyptogena* or other chemosynthetic bio-communities orientations indicate the existence of a strike-slip stress regime with a vertical direction of σ_2 (Fig. 1.2). Ogawa and Asada (2009) presumed that the proto-thrust zone and decollement

have high permeability in the σ_2 direction. The hydraulic gradient may be occasionally caused by or modified by thermal pressurization during seismic rupturing (Wibberley, 2002) and/or over-pressurization due to methane hydrate dissociation (Holtzman and Juanes, 2011) in the accretionary prism.

Computer simulations are generally used in estimating subsurface fluid migration; however, it is important to input accurate hydraulic constants such as permeability and specific storage. Hence, the reliability of groundwater flow analysis depends on the accuracy of acquired hydraulic constants for the considered underground environment. Acquiring such parameters through *in-situ* measurements from deep underground or under the seafloor is difficult because of the requirement for drilling technology and the associated time and cost constraints. Thus, it is crucial to measure physical parameters such as strength and hydraulic constants of rocks through laboratory experiments, assuming an underground stress state. There are three broadly used laboratory experimental techniques to obtain mechanical properties and hydraulic constants of rocks in the previous studies. Permeability measurements have been conducted under:

1) isotropic confining pressure,

2) uniaxial compressional and/or extensional stresses through conventional triaxial test,

3) triaxial stresses through true triaxial test.

All of these measurements aimed to understand permeability changes during deformation under an underground environment. The confining pressure technique (1) implies an isotropic stress condition where the same pressure is applied to all sample surfaces. In natural underground conditions, the confining pressure is equivalent to lithostatic pressure resulting from the load of overlying rocks and fluids. In experimental study, the confining pressure is a hydrostatic pressure, generally produced by fluid. In the conventional triaxial test technique (2), axial stress, usually generated by a pair of rigid piston cylinder, is applied to a cylindrical rock specimen to the failure at a certain confining pressure. The stress state of subduction

zones is affected not only by overlying pressure but also horizontal compression by plate tectonics. Conventional triaxial tests are used to define criteria for the rock failure. The true triaxial test (3) allows independent control of stresses applied in three dimensions to a rectangular prismatic rock specimen. The true triaxial test, which can simulate three dimensional stresses, is the most effective experimental method for obtaining the deformation property of rocks.

In this chapter, the purpose of this study is described after discussion previous studies, considering the advantages, problems and difficulties associated with evaluating the permeability of rocks. In Section 1.1, the methods of permeability measurement are described. Then in Section 1.2, a summary of previous studies of permeability measurement that use above three laboratory experimental techniques is presented. In Section 1.3, the purpose of this study is described based on the outcomes of the review sections. Finally, the main components of this thesis is summarized.

1.1 Previous studies on permeability measurement of rocks

Permeability of rocks primarily depends on the average size and connectivity of pores and the throats that connect the individual pores. Factors of pore size and distribution are dependent on the particle size and shape and the degree of sorting. Since the permeability of rock is directly affected by the pore networks, increasing stress on rock causes permeability reduction. Permeability anisotropy can be produced through the formation of oriented fabrics and foliations during deposition and deformation or through the preferential orientation of pore connectivity during deformation. Increasing porosity occurred as a result of the development of fractures with stresses. Decreasing porosity occurred as a result of cataclasis, pore collapse and cementation. Under experimental study, crystalline rocks show permeability that increases over two orders of magnitude up until rock failure (Mitchell and Faulkner, 2008). The degree of permeability anisotropy is between one to three orders of magnitude

from faulted porous sandstones with anisotropy of two orders of magnitude in the majority of samples taken within 10 cm of the fault plane (Farrell et al. 2014). Accordingly, when permeability measurements are conducted during deformation, appropriate methods should be chosen. There are four main permeability measurement methods: the constant head method, falling head method, flow pump method and transient pulse method. Each of the following sections explains the details of each method, and then describes which of the methods is most appropriate for this study.

1.1.1 Constant head method

The constant head method can be used to measure permeability of coarse grained soils such as gravelly sand and coarse and medium sand under low water head (Fig. 1.3). In 1856, Henry Darcy published a relationship for the flow rate of water in sand filters for the municipal water system (Brown 2002). In the constant head method, the water head between the upstream reservoir and downstream reservoir is conserved. The relation between the flow rate and differential water head is called Darcy's Law, written as follows:

$$Q = KA\frac{h_u - h_d}{l},$$

where Q is the volume flow rate, A is the area of specimen, K is permeability, h_u and h_d are the water head of upstream reservoir and downstream reservoir and l is the length of the specimen.

1.1.2 Falling head method

The falling head method can be used to measure permeability of fine-grained soils such as clayey or silty soils. This method involves flow of water through a specimen connected to a standpipe which provides the water head and also allows measurement of the volume of water passing through the specimen (Fig. 1.4). On the basis of the test results, the permeability of the specimen can be calculated as:

$K = \frac{al}{At} ln \frac{H_u - h_d}{h_u - h_d}$,

where *t* is the recorded time, H_u is the water head at initial value of experiment and a is the cross-sectional area of the stand pipe.

1.1.3 Flow pump method

The flow pump method proposed for low permeability clay specimen by Olsen (1966). The essential difference between this method and the constant head method is that the flow rate is controlled to ensure constant head by using the water supply syringe pump. Accordingly, permeability can be calculated using Darcy's Law in equilibrium pressure state. In addition, a wide range of permeability can be measured by the flow pump method because the pore pressure is controlled by the flow rate control syringe pumps that have high resolution pressure gauges. Theoretical analysis of the flow pump method was developed by Morin and Olsen (1987) by analyzing the transient response obtained from the test to determine the permeability and storage capacity of the specimen. Later, Esaki et al. (1996) and Zhang et al. (2000) proposed a numerical technique to obtain the permeability, specific storage of the sample and the storage capacity of the flow pump apparatus by applying a non-linear least-square minimization algorithm. However, as Zhang et al. (2000) mentioned, specific storage is less sensitive than permeability, suggesting that the quality of the values obtained by this method can vary significantly. Tokunaga et al. (2003) suggested that the ratio of the storage capacity of the apparatus to that of the specimen should be less than a certain reference value 0.3 to obtain a reliable data. In the current study, the flow pump method was the main method used to obtain permeability and the specific storage of specimens. Therefore details of the calculation will be described in Chapter 3.

1.1.4 Transient pulse method

The transient pulse method originally introduced to measure the permeability of the rocks

with low permeability by Brace et al. (1968). In their procedure, a small transient pulse pressure was applied to the upstream reservoir and the pressure decay curve was observed as the pore fluid conduction through the specimen (in their case, the Westerly granite) from the upstream reservoir to downstream reservoir. The main advantage of the transient pulse method is that it is relatively quick to analyze the permeability value for low permeability specimens. The equation shown by Brace et al. (1968) is as follows:

$$\frac{h_u - h_d}{H} = exp\left\{-\frac{KAt}{l}\left(\frac{1}{S_u} + \frac{1}{S_d}\right)\right\},$$

where H is the pulse pressure, and S_u and S_d are specific storage of the upstream reservoir and downstream reservoir of the apparatus, respectively. Based on numerical solutions, Lin (1977) and Hsieh et al. (1981) showed that Brace's equation can lead to a significant error caused by storage capacity of apparatus. Hsieh et al. (1981) suggested an improved solution of the transient pulse method, considering the storage capacity of apparatus.

1.1.5 Permeability measurement method for deforming specimen

An approximation of applicable range of permeability for each method is listed as follow by Lin et al. (2003), based on the compilation of previous studies:

Constant head method: 10^{-3}–10^{-12} m/s

Falling head method: 10^{-4}–10^{-11} m/s

Flow pump method: 10^{-4}–10^{-14} m/s

Transient pulse method: 10^{-8}–10^{-14} m/s

The permeability of sedimentary rocks such as sandstone and mudstone ranges 10^{-6}–10^{-12} m/s. The current study focuses on permeability change and/or permeability anisotropy during deformation, therefore there is some possibility of drastic change of permeability. Consequently, the flow pump method was chosen for permeability measurement under the true triaxial test as it should be able to measure the expected wide range and low permeability. The constant head method is also useful; however, the pore pressure has been shown not to be

sufficiently stable compared with the flow pump method, based on experience.

1.2 Stress dependency of permeability

1.2.1 Effective confining pressure dependence

A wide range of permeability for rocks under confining pressure conditions has been reported by numerous previous studies, which aimed to estimate the underground hydraulic structures. In recent years, many researches have also focused on stress dependency of permeability for application purposes to extraction of coal bed methane resources (Meng and Li, 2013), or understanding hydraulic barriers in water reservoirs, and waste containmination processes of environment by wastes (Dafalla et al. 2015; Fujii et al. 2015).

Permeability measurements under the isotropic confining pressures show that permeability decreases with increasing confining pressure in Westerly granite (Brace et al. 1968), Inada granite (Takahashi et al. 1990), and fault related rocks (Evans et al. 1997; Wibberley and Shimamoto, 2003). Increasing effective confining pressure on rock causes permeability reduction by changing pore networks (Brace. 1980; Walsh et al. 1981). In addition, it is well recognized that permeability and porosity of sedimentary rocks depend not only on the loading condition, but also on the stress history the sedimentary basin underwent (Kwon et al. 2004; Dong et al. 2010). Dong et al. (2010) conducted permeability experiments by first gradually increasing the confining pressure from 3 to 120 MPa and then subsequently reducing it back to 3 MPa using sedimentary rocks recovered from a 2000 m-deep borehole. They showed that permeability of the sandstones remained within a narrow range, whereas the permeability of the shales was more sensitive to the effective confining pressure, and varied from two to three orders of magnitude possibly due to the existence of microcracks in the shales. Fujii et al. (2015) agreed that the significant permeability reduction could be attributed to the presence of crack-like pores and microstructures by measuring permeability

for mudstones, which have various different grain sizes.

1.2.2 Shear deformation dependence

When measuring permeability under conventional triaxial stress, a cylindrical rock specimen is loaded axially to failure at a confining pressure. Permeability experimental studies were conducted during conventional triaxial compression ($\sigma_3 = \sigma_2 < \sigma_1$) and extension ($\sigma_3 < \sigma_2 = \sigma_1$) using the cylindrical specimens of weakly-cemented sandstones (Zoback and Byerlee, 1976), or porous sandstone including Berea sandstone (Zhu et al. 1997; 2002). Zhu et al. (2002) showed permeability parallel to the direction of σ_1 is generally higher than in the direction of σ_3. Thin sections made from deformed samples revealed significant cataclasis in samples taken at high confining pressure conditions for Berea sandstone (Menéndez et al. 1996) and for Darley Dale sandstone (Wong and Baud. 1999), which probably have resulted in permeability anisotropy (Zhu et al. 2002). Permeability anisotropy produced by cataclasis is also observed from ring shearing tests with artificial quartz gouge (Zhang and Tullis. 1998). Zhang and Tullis (1998) identified permeability anisotropy of one order of magnitude with high permeability parallel to the fault plane and low permeability perpendicular to the fault plane. They suggested that the magnitude of permeability anisotropy depends on the degree of shear localization.

Recent research efforts focused on permeability change during deformation has also conducted using improved conventional triaxial experimental methods. Permeability measurements during cyclic loading conditions were performed to investigate cumulative damage and permeability hysteresis of Cerro Cristales granodiorite and Westerly granite (Mitcell and Faulkner, 2008). Many similarities between granodiorite and granite were shown by the permeability results, which include an initial transient permeability decrease with increasing differential stress and strain that was more prominent for the granodiorite than the granite. They suggested that the initial permeability decrease is related to the nonlinear

increasing stiffness part of the stress-strain curve, most likely due to the closure of microfractures oriented obliquely and transversely to the applied load. At post-failure, the permeability increased one to three orders of magnitude relative to the initial permeability. Mitchell and Faulkner (2008) showed increasing permeability with failure of the specimen and a larger increase in porosity for the granite in comparison to those for the granodiorite. Furthermore, the total change in permeability was similar to the total change of the non-cycled experiments and permeability was primarily controlled by the total σ_1 that the specimen experienced, rather than number of cycles. Chen et al. (2014) also confirmed that the permeability properties of damaged rock are strongly influenced by the initiation and growth of microcracks by hydro-mechanical coupling during compressive deformation and development of the damage zone of granite.

Alam et al. (2014) conducted permeability measurement on several kinds of rocks (Shikotsu welded tuff, Kimachi tuffaceous sandstone and Inada granite) and reported their structural changes using thin section analysis and X-ray CT. For the Inada granite, their results of permeability behavior during axial compression were almost the same as the results of Mitchell and Faulkner (2008). For tuffaceous sandstone, the permeability decreased with increasing σ_1, and thence began to increase with increased σ_1 loading, and finally showed an almost constant value in the post-failure. Alam et al. (2014) attributed the decreasing permeability at initial loading mainly to either compaction or plastic deformation of clay cementing materials of tuffaceous sandstone. In the case of welded tuff, the permeability monotonously decreased with σ_1 loading caused by pore collapse.

Previous studies mainly suggested that the permeability properties during σ_1 loading were related to specimen strength and initial pore structures. Cataclasis and pore collapse cause permeability decrease, and growth of microcracks causes permeability increase under conventional triaxial tests.

1.2.3 Permeability measurements under true triaxial tests

The true triaxial test, which can simulate *in-situ* stress fields of nature which have different scalar quantity along three principal axes of stress, is the most effective experimental method for obtaining the mechanical and permeability property of rocks under tectonic stresses. Mogi (1970) first implimented the application of three mutually independent and uniform loads to the specimen faces, and thus this method is called Mogi-type. Mogi-type true triaxial tests apply two stresses by rigid platens and the other by oil pressure. Takahashi et al. (1993; 1995) investigated the effects of three principal stresses on permeability in the σ_1 direction for Shirahama sandstone using Mogi-type true triaxial test apparatus. Their results showed that the effect of σ_1 is more significant than that of σ_2. Li et al. (2002) measured permeability along σ_2 direction to assess the effects of three principal stresses on permeability using Mogi-type true triaxial tests apparatus for Shirahama sandstone. The permeability is independent of stress states and loading paths under monotonic loading within elastic deformation.

King et al. (1995) conducted permeability measurements for cubic specimens of initially isotropic cracked sandstones while differential stresses were applied by three pairs of rigid platens (called rigid platen type), and investigated the effect of the stress perpendicular to the crack plane on the permeability. Nasseri et al. (2014) carried out three directional permeability ans ultrasonic wave velocity measurements, and acoustic emission measurements using a in rigid platen type true triaxial apparatus for two cubic specimens. Comparison of the variation of three directional permeabilities between the specimens showed that higher magnitude of σ_3 and σ_2 disrupts the pore spaces, irrespective of the magnitude of the applied stress ratio of σ_2/σ_3. The observed permeability anisotropy between the two specimens is a function of inherent oriented pores and cracks, stress ratio of σ_2/σ_3 and the magnitude of applied σ_3 and σ_2 stresses. The experimental technique of Nasseri et al. (2014) is advantageous in that it can obtain substantial information for physical properties under true triaxial tests; however, the

effect of the stresses is not clear because of the limited number of tests.

1.3 Objective

Previous studies using true triaxial test apparatus have revealed that σ_2 has the major control on fracture strength, mechanical behavior and crack distribution. It is clear that permeability is also dependent on the σ_2 value under constant σ_3 conditions; however, no previous study has measured the permeability of σ_1 and σ_2 directions simultaneously for sufficient repeatability under the above stress states. The objective of this study is to evaluate the permeability change and permeability anisotropy for sedimentary rocks under true triaxial stresses.

1.4 Summary of Contents

Chapter 1 describes the background of the present study and objective.

Chapter 2 proposes the requirements for deformation properties of submarine sedimentary rock. Submarine sedimentary rocks have a wide range of compressive strength and permeability properties depending on the consolidation, cementation and rock type. For the purpose of understanding the relationships between compressive stress and deformation property, conventional triaxial tests are conducted on artificial unconsolidated to partially consolidated sediments (mixed cement with sands). The deformation type, opening shear fracture or coherent shear band was controlled by pre-consolidation pressure and/or confining pressure.

Chapter 3 first considers the data acquisition method for obtaining fundamental permeability parameters. Then, the experimental evaluation of hydraulic constants in mudstone using the flow pump method is indicated. An improved experimental method is

developed to obtain more accurate values of specific storage of specimens, considering the error range.

Chapter 4 presents the results of permeability measurements for sedimentary rocks using Mogi-type true triaxial test apparatus. These results suggest that σ_2 controls the mechanical behavior and crack distribution of deformed rocks under constant σ_3 conditions. Thus, the permeability anisotropy caused by fault gouge was observed at higher σ_2 conditions.

Chapter 5 presents the application of permeability measurement under true triaxial stresses for modelling of accretionary prism.

Finally, Chapter 6 summarizes the conclusions obtained from the present study.

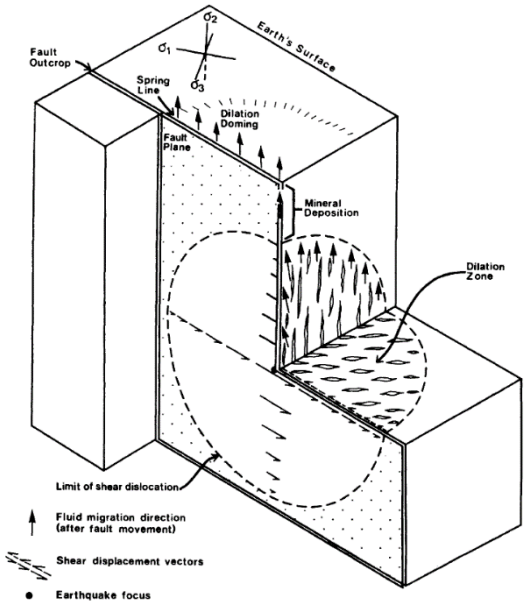

Fig. 1.1 Fluid flow toward σ_2 in the strike-slip stress regime with pressure relief after shallow earthquake (Sibson et al. 1975).

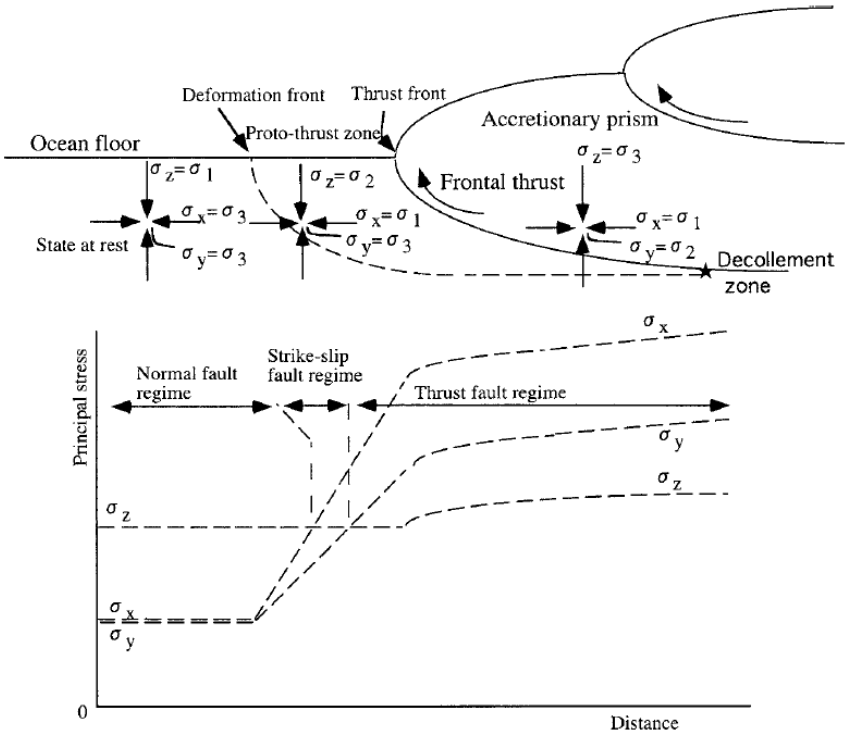

Fig. 1.2. Simplified schematic diagram of the site of stress regime in the accretionary prism (Ogawa et al. 1996). The principal stress axes are assumed either to be vertical or horizontal.

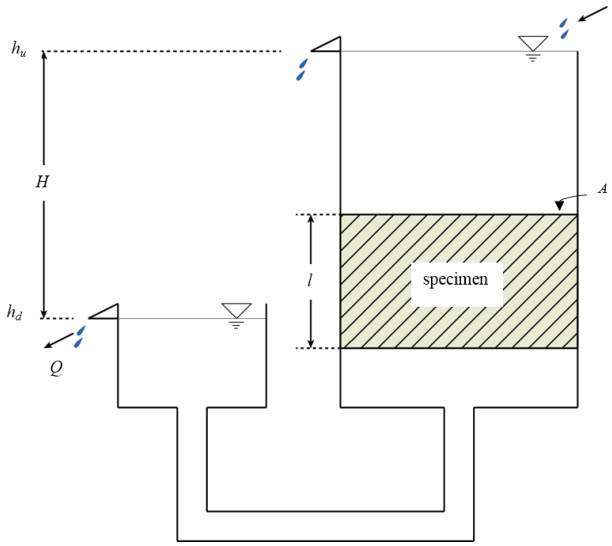

Fig. 1.3 Schematic diagram of constant head method. Q is the volume flow rate, A is the are of specimen, h_u and h_d are the water head of upstream reservoir and downstream reservoir, H is the differential head and l is the length of the specimen.

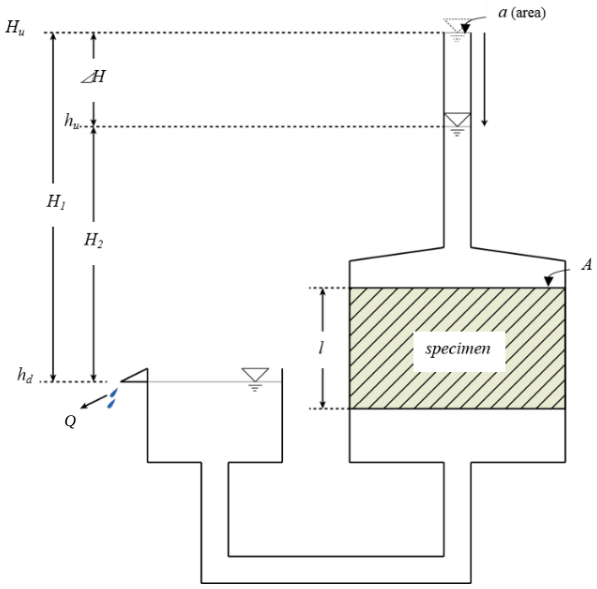

Fig. 1.4 Schematic diagram of falling head method. Q is the volume of flow rate, A is the area of specimen, a is the crosss-sectional are of stand pipe, H_u is the water head at initial value of experiment, h_u is water head at t (time), h_d is the water head of downstream reservoir, H_1 and H_2 are the differential head at initial value and at t and l is the length of the specimen.

2. Physical and deformation properties of artificial specimens

2.1 Introduction

Permeability properties of sedimentary rocks are largely dependent on shear fractures and faulting. Field studies of accretionary prisms have suggested that Calyptogena or other chemosynthetic bio-communities form en échelon assemblages, reflecting underlying fracture patterns. The fluids containing methane and/or other nutrients seep through these fractures and support the lives of chemosynthetic bio-communities (Ogawa et al. 1996). Estimation of the fluid migration of accretionary prism is important; however, there are some limitations to acquiring *in-situ* data from subsurface or below deep sea environments. Therefore, simulation experiments are generally required to understand the physical properties below the seabed in deep sea regions.

The results of ring shearing tests by Zhu and Tullis (1998) identified permeability anisotropy of one order of magnitude with high permeability parallel to the fault plane and low permeability perpendicular to fault plane. Here, it is crucial to understand that permeability has anisotropic properties. Moreover, it is necessary to consider which conditions of strength or type of sample and/or compressive stress cause effectively to faulting lead the barrier or channel of fluid flow.

This chapter describes experiments for obtaining physical and deformation properties of artificial unconsolidated to partially consolidated sediments (mixed cement and sand) that were conducted under various stress conditions. The key advantage of testing artificial samples is sthe enhanced repeatability. Firstly, the physical and deformation properties of artificial specimens were investigated under several stress and strength conditions using conventional triaxial tests. Next, the deformation of the internal structure of artificial specimen was observed by micro-focus X-ray CT. The experimental procedure of this study is written Sato et al. (2013).

2.2 Experimental procedure

2.2.1 Preparation of artificial specimens

For the simulation of the strength of submarine sedimentary rocks, artificial specimens were made by mixing Futtsu sand (from Chiba, Japan) and Ordinary Portland Cement. Skeletal density of Futtsu sand was 2.66, and that of Ordinary Portland Cement was 3.08, measured using a gas pycnometer (Accupyc 1330; Micromeritics, Fig. 2.1). This instrument determines the skeletal density and volume of a sample by measuring the pressure change of helium in a calibrated volume.

The particle size distribution of sand and cement were measured using a laser diffraction particle size analyzer (SALD-3000s; Shimadzu Co., Ltd, Fig. 2.2). Fig. 2.3 shows the particle size distribution of sand and mixed samples (calculated from the mixed weight rate). The median diameter of sand is 0.3 mm and that of cement is in the 0.05 mm. With increasing mixing cement weight rate, the percentage of smaller particles increases. The particle size distribution of mixed particles is similar to that of the specimen selected from the sediments of methane hydrate stability zone of submarine sedimentary rocks (Nishio et al. 2003). Using the artificial specimen mixed sand and cement, we are able to simulate the submarine sedimentary rocks containing methane hydrate and/or the cementation.

First, 900 g sands and cement were mixed in container, making three identical specimens each time. The selected amounts of cement were 60, 120 and 180 g (giving a percentage of cement of 6.3%, 11.8% and 16.7%, respectively). Second, distilled water was added 10 g at a time and mixed equally. The mixed sample was placed into a mold (50 mm internal diameter, 100 mm height) divided five times. Next, the samples were compacted 15 times using a 2.5 kg rammer (Fig. 2.4). Excess mixed particles were removed and the curing period of compacted samples were cured for 7 days. Fig. 2.5 shows the finished specimen for the

conventional triaxial test. Specimens of the 6.3%, 11.8%, 16.7% cement rate are named Specimen A, Specimen B and Specimen C, respectively.

2.2.2 Experimental equipment

The tests were conducted using the conventional triaxial compression test apparatus of the Department of Geosystem Science, Nihon University of Japan (Figs. 2.6 and 2.7). The stresses of $\sigma_2 = \sigma_3$ were applied by oil pressure to the cylindrical specimen, and σ_1 was applied by rigid piston in the axial direction. The test apparatus contains a pressure vessel, axial loading system, rigid piston, load cell, hand pump for controlling confining pressure, local deformation transducer (LDT), displacement meter for axial direction, amplifier for the displacement meter and LDT, and a computer to act as a recording device.

The specimen was placed between the endpieces and was jacketed by rubber to eliminate oil injection into the specimen. The contact plane of endpieces to specimen were made of porous metal for drainage during compression. The specimen was set on the bottom of the pressure vessel and LDTs were attached to the side surface of the specimen. After setting the pressure vessel, oil for isotropic confining pressure was filled into pressure vessel. Axial stress (σ_1) was loaded at constant strain rate (1.25×10^{-4} s^{-1}) under constant confining pressure ($\sigma_2 = \sigma_3$).

Conventional triaxial tests were conducted on Specimens A and B at confining pressures of 0.2, 1.0, 2.5, 5.0 and 7.5 MPa. Tests were conducted on Specimen C at confining pressures of 1.0, 2.5, 7.5 and 10.0 MPa. All tests were conducted in the consolidated–drained (CD) condition at room temperature.

2.3 Results

2.3.1 Results of the conventional triaxial test

Fig. 2.6 shows the differential stress versus axial strain curves and volumetric strain versus

axial strain curves from conventional triaxial tests for the artificial specimens. Positive direction of strain axis generally represents the compressional direction in the field of rock mechanics. For example, in the results of Specimen A in the lower graph of Fig. 2.6, black circles show the volume increase with compression in the σ_1 direction. This means the total circumferential strain expansion quantity is larger than compression quantity of σ_1 direction. The results of the upper graph in Fig. 2.6 show that differential stress increased with increases of the function of confining pressure. In addition, the curves describe the transition from brittle deformation with stress drop to ductile deformation with strain hardening. The lower graph of Fig. 2.6 shows initial compression of volumetric strain; however, after the yield point, volumetric strain expanded with increased σ_1 loading.

Fig. 2.7 shows the photos and soft X-ray CT images of Specimen C after conventional triaxial tests. In the soft X-ray CT images, white color means high density and black means low density. In the case of deformation under 2.5 MPa, shear band is opened with partially coherent. However, in the case of deformation at under 5.0 MPa, the shear band is coherent at 7.5 MPa, shear band is not clear and density deferences cannot be observed.

2.3.2 Observation of internal structure of the deformed specimen

It is important to understand the permeability of deformation bands, whether opening shear fractures or coherent shear bands. This study observed internal structure of deformed Specimen C after a confining triaxial test at 5 MPa confining pressure using micro-focus X-ray CT. A 10 mm diameter cylindrical specimen was cored from deformed specimen, which was fixed by epoxy resin. The cylindrical specimen for CT analysis was cored perpendicular to the shear band (Fig. 2.8). The tomography system used the HMX225 system (Tesco Corporation) to obtain micro-focus X-ray CT images. The set values of acquiring X-ray images are summarized in Table 2.1. Cross-sectional X-ray images and attenuation coefficients of all images were acquired by the system. Whether pore or grains are

distinguished for binarization using effective porosity data, which was measured by the Vernier calipers method. The effective porosity of Specimen C was 36%. In addition, two 2 × 2 × 2 mm cubes representing 1) coherent shear band and 2) areas adjacent to the coherent shear band were extracted from the three dimensional volume data (Fig. 2.8).

The three dimensional visualization data were composed using software (ExFact Analysis, Nihon Visual Science). From the binarization of cubic data, the porosity of both cubes were calculated by amount of pore volume voxels. The porosity of coherent shear band was 15.4% and that of adjacent to coherent shear band was 36.0%. Therefore, the porosity of coherent shear band was lower than that adjacent to the coherent shear band by 20% porosity.

Tortuosity was evaluated to three directions of the two cubes. Tortuosity is widely used in petrophysics, as one of the parameters that make up formation factors in Archie's empirical law relating the porosity and brine saturation of rocks to their electrical conductivity (Archie, 1941).

The definition of tortuosity is given by:

$$\tau = \frac{L}{L_0},$$

where L is the apparent length of element and L is the length of fluid flow path through the porous matrix (Fig. 2.9). With increasing values of tortuosity, the porous matrix becomes more complicated. If considering fluid flow in porous matrix, the value of tortuosity becomes meaningful for permeability.

The X and Y axis are parallel to the shear band, and Z axis is perpendicular to the shear band. Fig. 2-10 shows tortuosity versus probability density of each cube. The tortuosity of adjacent shear band cube protuberate around 1.7. In contrast, the tortuosity of the shear band cube, high tortuosity (> 2.0) of the probability density is more than adjacent shear band cube. Furthermore, in the shear band cube, the probability density of the Z direction is higher than that of the X and Y directions.

After the micro-focus X-ray CT, thin sections of the shear band and adjacent to the shear

band were made from the same deformed specimen. Grain crashing was not observed in either of the thin sections. Accordingly, porosity reduction may be caused by the reorientation of sand and cement particles in the specimen.

2.4 Discussion

Previous studies mainly suggested that the permeability properties during σ_1 loading were related to specimen strength and initial pore structures. Cataclasis and pore collapse cause decreasing permeability, and growth of microcracks causes increasing permeability under conventional triaxial tests. In this study, pore collapse with reorientation of sand particles, porosity reduction and tortuosity anisotropy were observed in the coherent shear band deformed specimen. The results mean the permeability reduction and permeability anisotropy was occurred in the coherent shear band in deformation specimen. However, permeability measurement was not able to conduct in this test. Then, it is necessary to measure the permeability of rocks during deformation, and next chapter introduces permeability measurements for sedimentary rocks.

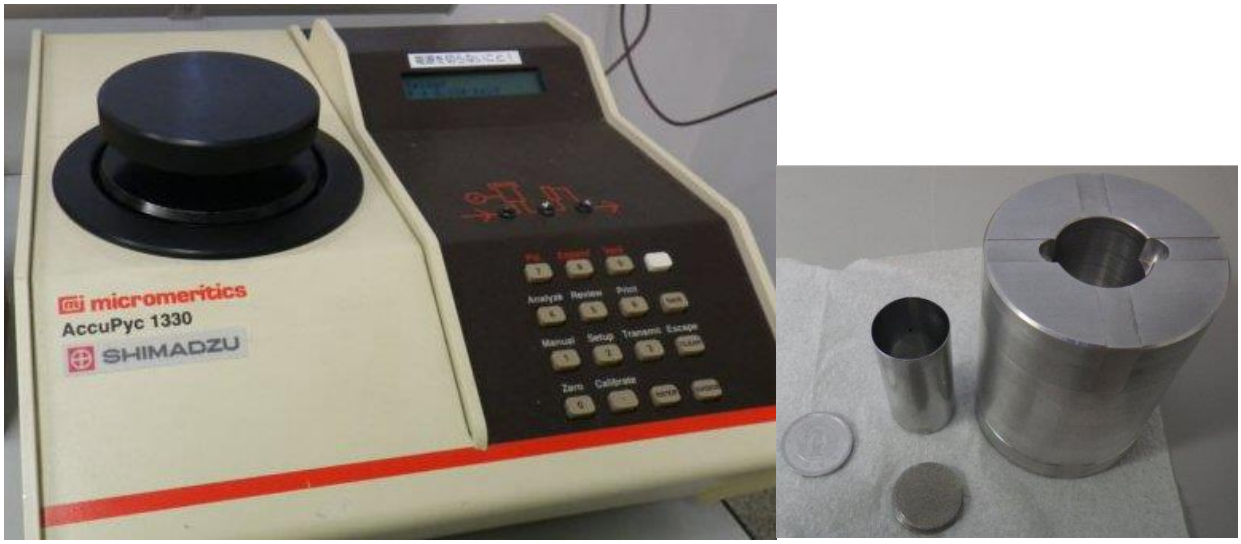

Fig. 2.1 Photograph of the Accupyc 1330 (Micromeritics) instrument (left) that determines the skeletal density and volume of a sample by measuring the pressure change of helium in a calibrated volume(a 10 cc cell for samples; right).

Fig. 2.2 Laser diffraction particle size analyzer (SALD-3000s; Shimadzu Co., Ltd.)

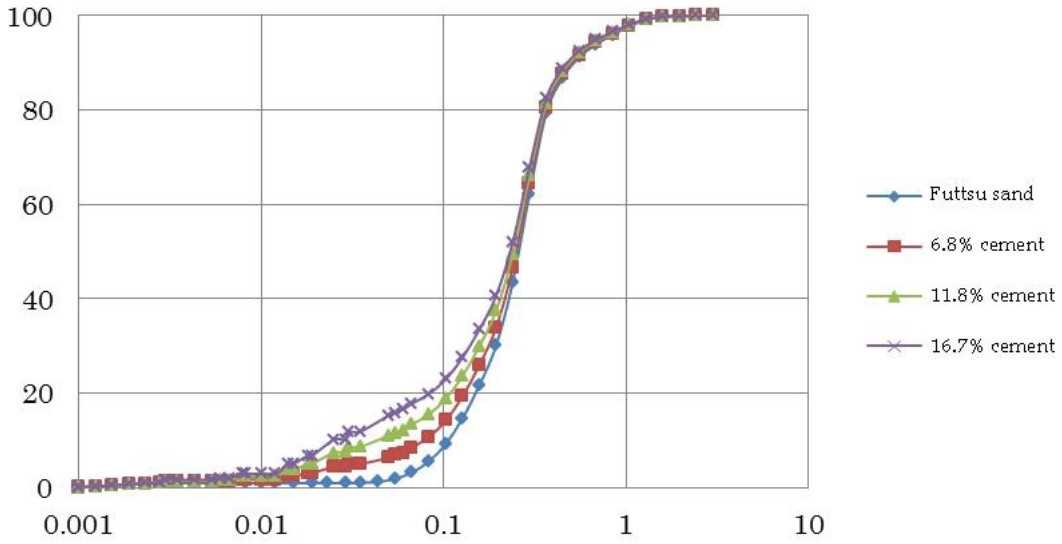

Fig. 2.3 Grain size distribution of Futtsu sand. Mixed samples were calculated from the mixed weight rate of sand and cement.

Fig. 2.4 Mold (left) and rammer (right) for compaction

Fig. 2.5 Finished specimen for conventional triaxial tests

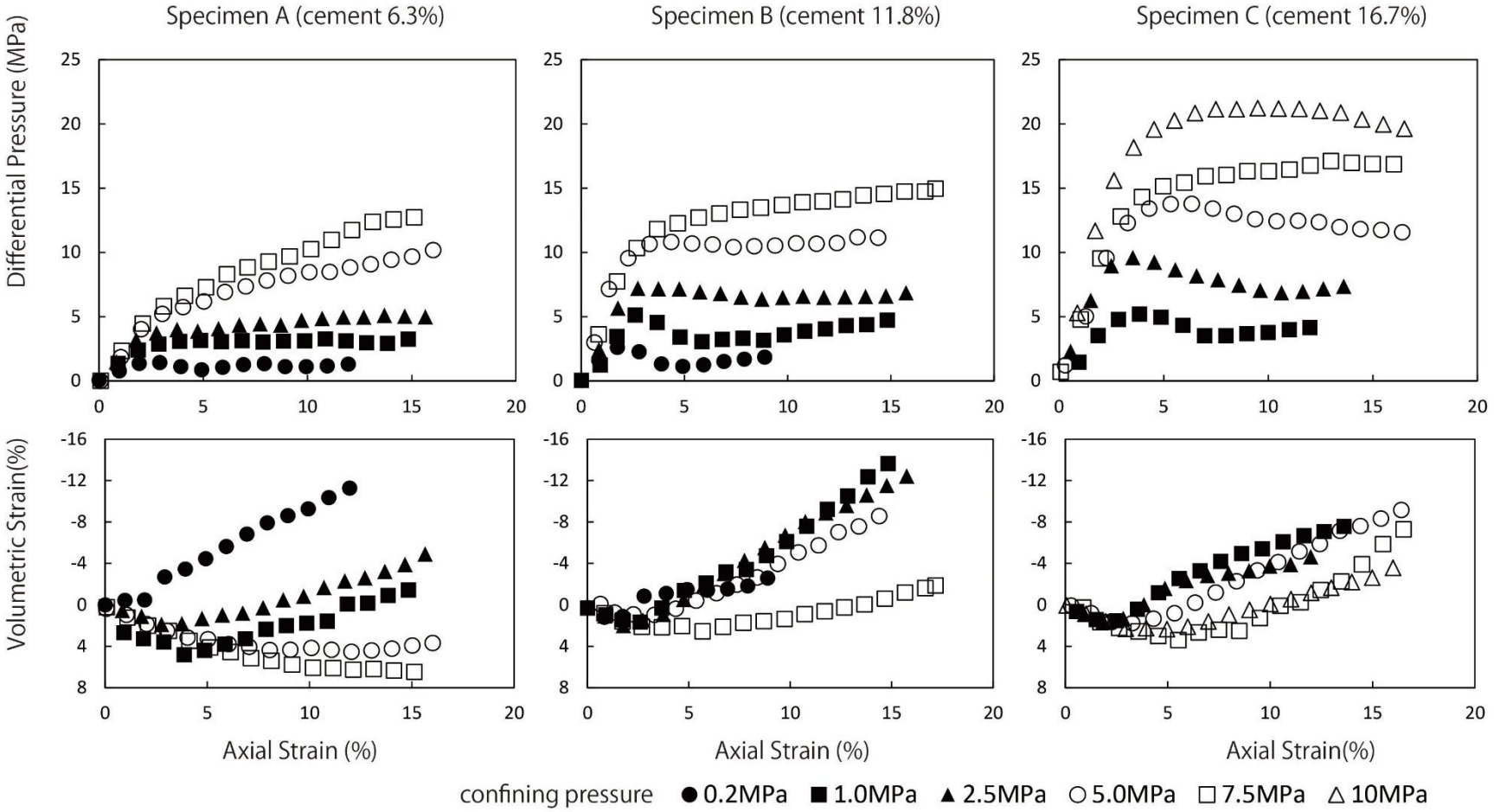

Fig. 2.6 Upper figure is axial strain versus differential pressure. Lower figure is axial strain versus volumetric strain.

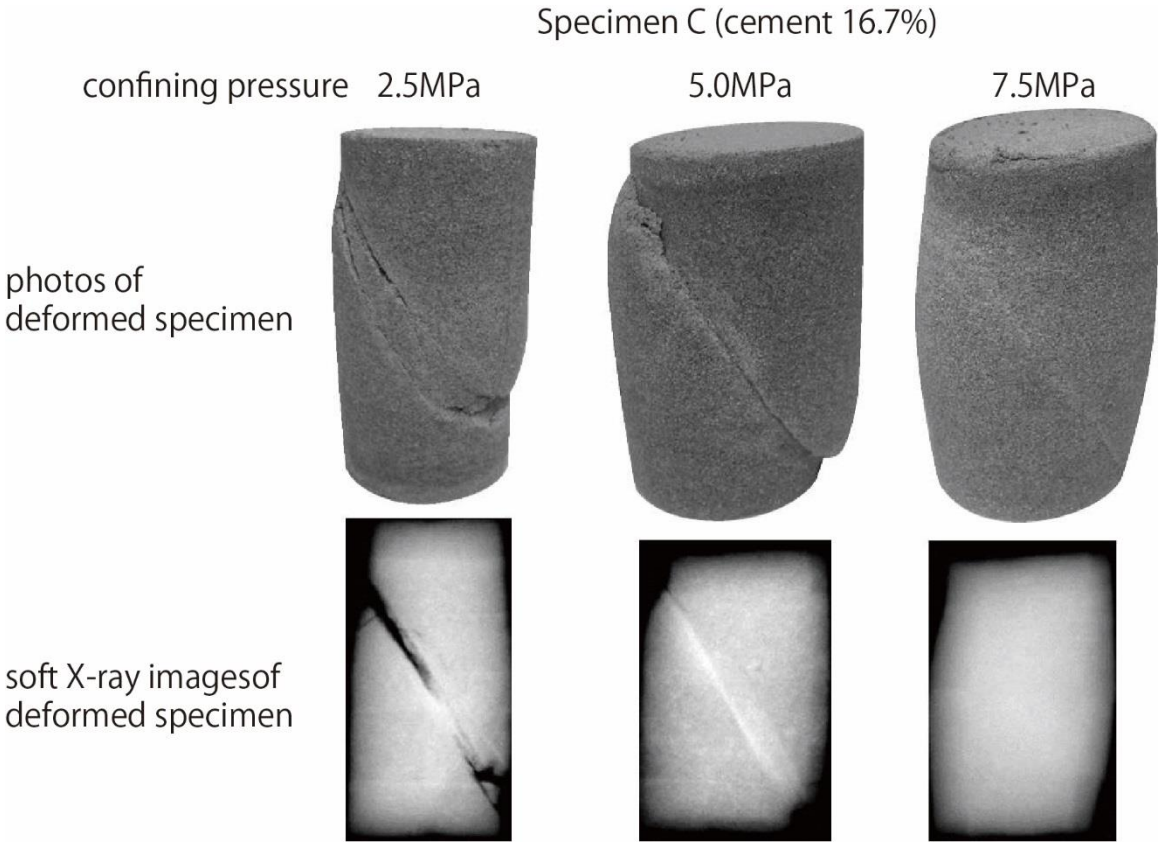

Fig. 2.7 Photographs and soft X-ray images of deformation Specimen C.

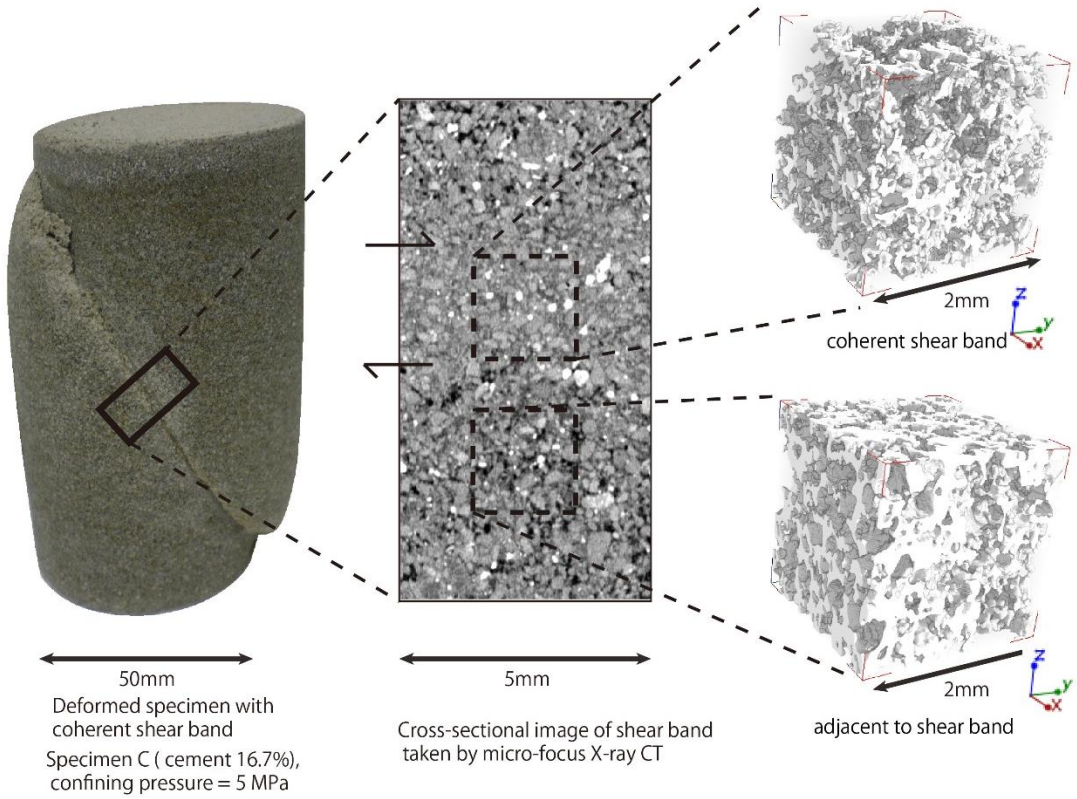

Fig. 2.8 Volume data of micro-focus X-ray CT of deformed specimen C. Left: photograph of deformed specimen. Center: Cross-sectional image of shear band taken by micro-focus X-ray CT. Right: Volume data of pore structure, where white represents the pore structure.

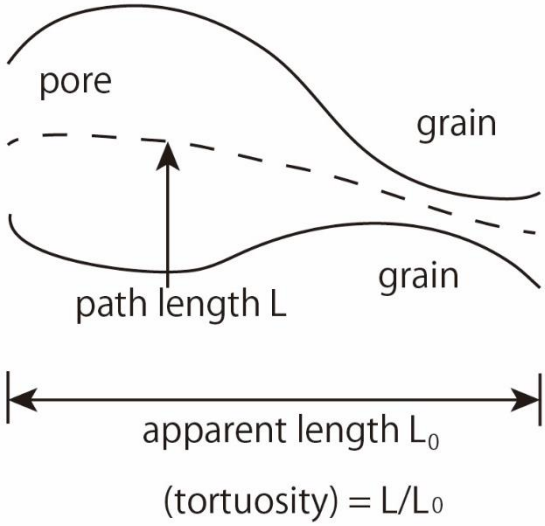

Fig. 2.9 Tortuosity of the porous matrix.

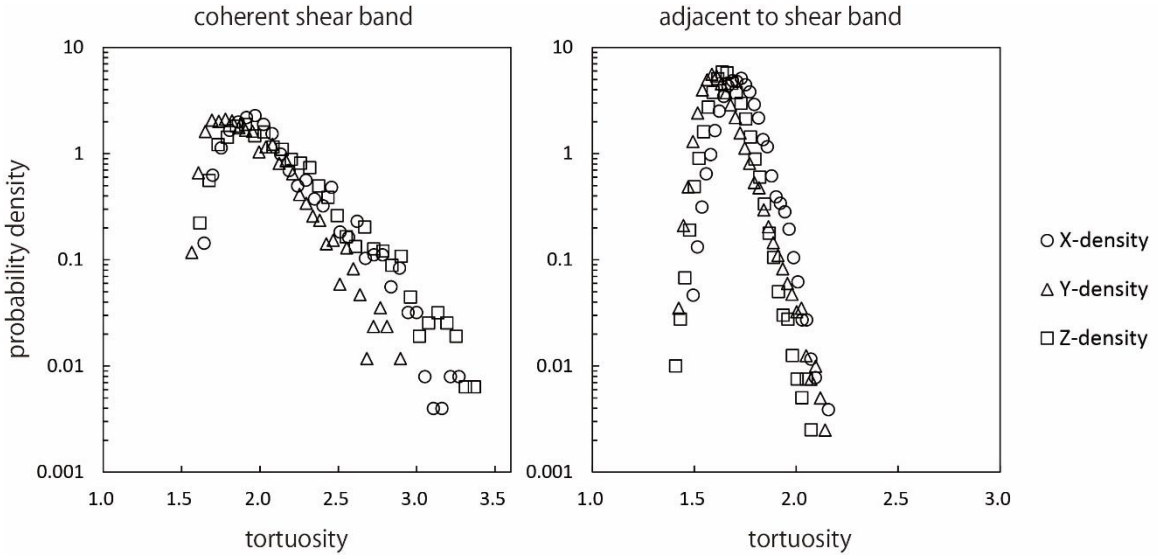

Fig. 2.10 Tortuosity distribution of deformed specimens.

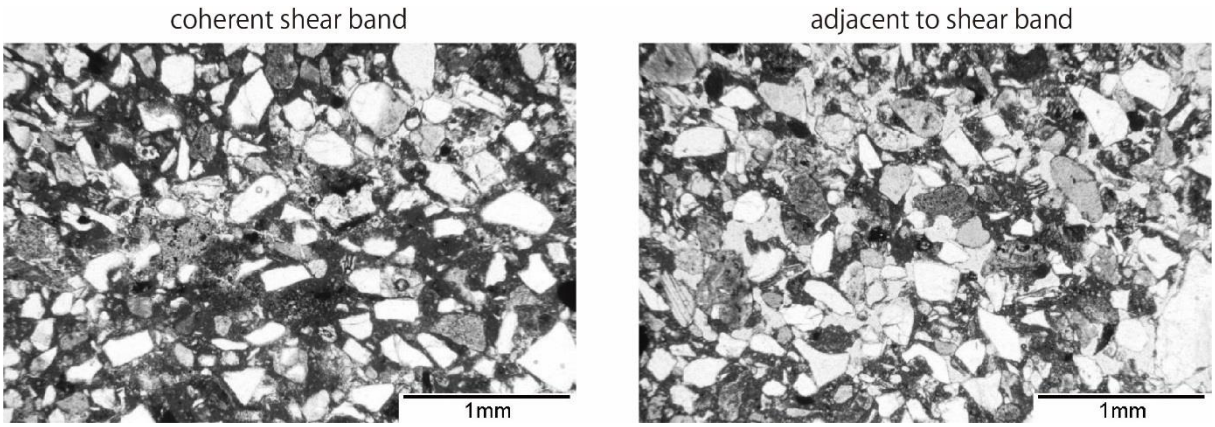

Fig. 2.11 Thin sections of the deformed specimen on the coherent shear band and adjacent to the coherent shear band.

3. Experimental Evaluation of Hydraulic Constants

3.1 Introduction

Several experimental methods for obtaining hydraulic constants have been proposed. These methods include the transient pulse method (Neuzil et al. 1981; Zhang et al. 2000; Kato et al. 2013), the flow pump method (Morin and Olsen. 1987; Esaki et al. 1996; Tokunaga and Kameya. 2003; Kameya and Tokunaga. 2003), flow pumping under a constant downstream reservoir volume (Song et al. 2006), and the poroelastic method in which strain and pore fluid pressure are measured in the specimen (Hart and Wang. 2001; Tokunaga et al. 2001; Tanikawa et al. 2008). For granite, with low hydraulic conductivity (lower than 10^{-10} m/s). Kato *et al*. (2013) summarized data analyses including sensitivities based on the nonlinear least-squares method and by the transient pulse method. Song *et al*. (2004) obtained the hydraulic conductivity and specific storage of specimens by a new flow pump measurement method under relatively constant downstream reservoir volume conditions. However, a constant flow rate from the upstream reservoir was observed to cause fluid to permeate into the specimen and the apparatus, leading to pore pressure increasing during measurements. Accordingly, the method of flow pump measurement under the constant downstream reservoir volume condition is not suitable for measurements under low effective confining pressures. Esaki *et al*. (1996) proposed an analytical solution for the conventional flow pump experiments that included the effects of the storage capacity of the flow pump apparatus. Tokunaga and Kameya (2003) also used an analytical solution for the flow pump method and conducted a theoretical analysis to evaluate errors associated with estimates of the specific storage of the specimen. Their results suggested that the ratio of the storage capacity of the apparatus to that of the specimen (δ') should be less than 0.3 for theoretical analyses and less than 0.7 for experimental results to obtain specific storage in the specimen with sufficient accuracy. Because the Wakkanai Formation mudstone in the Horonobe area is porous (porosity of about

30–40%), it is reasonable to assume that the value of δ' can be kept low using the flow pump method.

In the present study, ground water flow for a site in the Horonobe area was modelled. Because the hydraulic conductivity of the Horonobe mudstone within the Wakkanai Formation spans a wide range (10^{-14} to 10^{-6} m/s; Uehara et al. 2014), the flow pump method was chosen for this study. The flow pump method can handle wider ranges of values compared with the transient pulse method (Lin et al. 2003) and therefore facilitates for comparisons by providing the measurements. The experimental procedure of this study is written Sato et al. (2016). The flow pump measurements combined with an analytical method were employed to evaluate the possibility of obtaining accurate estimates of the specific storage of the mudstone in the Wakkanai Formation by comparing error ranges. Error ranges were calculated using an analytical solution based on a nonlinear least-squares method (Kato et al. 2013) to obtain the relative error.

3.2 Theoretical analysis

Flow pump experiments were performed by injecting distilled de-aired water at a constant rate from an upstream reservoir into the specimen using an ISCO syringe pump (100DM), and measuring the differential pressure between the top and bottom surfaces of the specimen (Fig. 3.1). The governing equation for one-dimensional fluid flow through a porous medium can be written as

$$\frac{\partial h}{\partial t} - \frac{K}{S'}\frac{\partial^2 h}{\partial x^2} = 0 \quad (1)$$

in which t is time, h is the hydraulic head, x is the coordinate with the origin 0 at the downstream end surface, S' is the specific storage of the specimen, and K represents hydraulic conductivity. x and t are independent variables in Eq. (1) for which the initial condition is:

$$h(x, 0) = 0, 0 \leq x \leq l \quad (2)$$

and in which l is the length of the specimen. The upstream boundary conditions are

$h(l,t) = h_u(t), t \geq 0$ (3),

and

$$\frac{S_u}{\kappa A}\frac{dh_u}{dt} + \left(\frac{\partial h}{\partial x}\right)_{x=l} = \frac{Q}{KA}, t > 0 \text{ (4)}$$

$h_u(0) = 0$ (5)

where S_u and h_u are the compressive storage and the hydraulic head of the upstream reservoir, respectively; Q is the constant pumping rate, and A is the cross-sectional area of the specimen. The downstream boundary condition is shown as follows:

$h(0,t) = 0, t \geq 0$ (6).

Finally, the analytical solution of Eq. (1) is [7]:

$$\frac{h(x,t)}{H} = \xi - 2\sum_{m=0}^{\infty} \frac{\exp(-\alpha\phi_m^2)\sin(\phi_m\xi)}{\phi_m\left(1+\beta+\frac{\phi_m^2}{\beta}\right)} \quad (7)$$

where α, and β are

$$\alpha = \frac{\kappa t}{l^2 S'} \text{ (8)},$$

and

$$\beta = \frac{S'Al}{S_u} \text{ (9)}$$

as non-dimensional parameters. The upstream (S_u) and downstream (S_d) compressive storage are:

$S_u = C_{ew}V_u$ (10),

and

$S_d = C_{ew}V_d$ (11)

in which C_{ew} is the compressibility of the apparatus as indicated by fluid flow lines. The ϕ are roots to the following nonlinear equation:

$tan\phi = \frac{\beta}{\phi}$ (12).

In this study, the analytical solution was used developed by Esaki et al. (1996) to obtain the hydraulic conductivity and specific storage of the specimens. In the calculations for error ranges, the analytical solutions based on the nonlinear least-squares method (Kato et al. 2013) was used. The hydraulic constants were determined by minimizing the residual sum of squares S as:

$$S = \sum_{i=1}^{n} \left[\frac{\Delta h^*(t_i)}{H} - \frac{\Delta h(t_i)}{H} \right]^2 \quad (13).$$

The relative errors of hydraulic constants were obtained using Eq. (13) for discussing the accuracy of obtained data. Finally, the error evaluation was apparent in the value of absolute errors calculated from relative errors.

3.3 Experimental procedure

3.3.1 Experimental equipment

The flow pump experiments were conducted using a triaxial vessel at the National Institute of Advanced Industrial Science and Technology of Japan (Fig. 3.2). The mechanism of this apparatus is basically the same as that of Kato *et al*. (2013). Three syringe pumps (ISCO, 100DM: maximum pressure of 69 MPa, controlling pressure resolution of 1 kPa, and flow range of 10^{-5} to 30 mL/min) were used to control pore fluid and confining pressure. This apparatus mainly consists of four systems to control pore fluid, confining pressure, and temperature along with a recording system. The control unit for confining pressure is composed of the pressure vessel (maximum pressure of 50 MPa) and syringe pump C (Fig. 3.2). The pore fluid system comprises syringe pumps A and B, a valve for separating upstream and downstream reservoirs, and fluid flowing lines. The recording system includes a data logger, a differential pressure transducer, and sensors to measure temperature. The temperature change in the heat insulated room 1 (Fig. 3.2) was kept within ± 0.1 degree during each experiment.

The cylindrical specimen (50 mm in diameter) was geared in endpieces that were equipped with a water distribution board and O-ring. After jacketing the specimen in a heat shrinkable tube, the specimen was placed on a disk-shaped piece of metal that bolts on to the pressure vessel. The lid and specimen were then turned upside down to be set into the pressure vessel. Once the above was assembled, the fluid could be supplied for the pore pressure and confining pressure tests.

Hydraulic constants were measured under isotropic stress conditions. The initial pressure for confinement was set as 4 MPa and pore pressure was kept constant at 2 MPa. Subsequently, confining pressure was incrementally increased from its initial value to 10 or 12 MPa, then later returned again at decreased step-sizes to the initial value. Because the limit for measuring differential pressure in the transducer was 140 kPa, flow pump experiments were conducted at differential pressures of less than 100 kPa to secure soundness of the equipment. Note that hydraulic constants were measured at each stage of the experiment.

3.3.2 Evaluation of the storage capacity of the apparatus

Because the flow pump experiments depend on the storage capacity of both the apparatus (S_u) and the specimen, it is necessary to discriminate between each type of storage to obtain an accurate estimate of the specific storage. Thus, it is better that the storage capacity of the apparatus is as small as possible (Esaki et al. 1996; Tokunaga and Kameya, 2003; Kameya and Tokunaga, 2003). A calibration test was conducted using an impermeable brass specimen to determine the storage capacity of the apparatus before doing permeability measurements. To do this, the storage capacity of the apparatus was obtained by measuring differential pressure changes with time under constant flow conditions, which is shown by:

$$S_u + S_d = \frac{Q}{\frac{\Delta h}{\Delta t}} \quad (15)$$

Both of the syringe pumps had volume of 10 mL. It should be emphasized that the same

systems were used for the upstream and downstream reservoirs and for adjusting the length of fluid flow lines; furthermore, it was assumed that $S_u = S_d$. Considering the aforementioned condition, a value of 2.34×10^{-10} m^2 was ultimately found for S_u in this study.

3.3.3 Specimen description

As briefly described earlier, core samples of mudstone from the Wakkanai Formation in the Horonobe area located in northern Hokkaido, Japan, were extracted for the experiments. The cores were obtained from borehole HDB4, previously drilled in the area by Japan Atomic Energy Agency (2003). Afterward, cylindrical specimens from the blocks were prepared in the laboratory using a diamond coring machine. The specimens had lengths ranging from 20–25 mm and a diameter of 50 mm, and were given the names HDB4-H223, V291, H291, H374 and H466. HDB stands for Horonobe Deep Borehole, and the numeral suffix (4 in this case) represents the site number. H and V stand for horizontal and vertical to the bedding plane, respectively, and the accompanying number refers to the depth of sampling (m). However, we used the intact specimen H374 as it was the only one with visible fractures (Fig. 3.3). The previously mentioned mudstone was chosen as a control measure as there are numerous reports available on the hydraulic conductivity of such rock, thus enabling an assessment of the reliability of measurements by comparing them with the previous work.

In subsequent stages, the porosity and pore size distributions of the specimen were obtained using mercury intrusion porosimetry (Fig. 3.4). The figure depicts pore volume per unit volume of the specimen in the vertical axis versus the logarithm of pore radii. All of the specimens had similar bimodal frequencies. The porosity of the specimen from 223 m is less than that of the specimen from 291 m. The porosity in other specimens tended to decrease with depth.

3.4 Experimental results

3.4.1 Measurement accuracy

At larger flow rate values, the equilibrium pressure increases. This can result in better measurement accuracy, because the equilibrium pressure highly exceeds the assemblage resolution. Hydraulic measurements of HDB4–H291, and H374 under various flow rate conditions were conducted to investigate the differences in measurement accuracy resulting from differential flow rate conditions (**Tab. 3-1**). For the same pressure conditions, there was a proportional relationship between flow rate and equilibrium pressure, as also could be shown with Darcy's Law. Because the limit for measuring differential pressure in the transducer was 140 kPa, the flow pump experiments were conducted at differential pressures of < 100 kPa to ensure that the equipment would not fail. For instance, because the first measurement was conducted under conditions in which effective confining pressure was 6 MPa and Q = 0.5 μL/min, the equilibrium pressure was 41.4 kPa. The second and third measurements were conducted based on Q = 10 and 11 μL/min, for which the equilibrium pressures were 78.5 and 90.7 kPa, respectively. Comparison of the equilibrium pressure under each pressure condition revealed that the error range value for the specific storage decreased as the flow rate increased. Then, the error range values of hydraulic conductivity were less than 1/10 of obtained hydraulic conductivity of the specimen.

3.4.2 Hydraulic conductivity

The initial permeability values for different specimens at the effective confining pressure of 2 MPa ranged from 10^{-8} to 10^{-12} m/s. The results of hydraulic conductivity versus effective confining pressure and error range bars are shown in Fig. 3.5. This figure was constructed using the most accurate measurements of differential flow rate conditions shown in Table 1, i.e., the results with the smallest error ranges. The error bars for hydraulic conductivity are

small enough to be hidden within the points plotted on the figure. Hydraulic conductivity was observed in all specimens to decrease with increasing effective pressure. During unloading, hydraulic conductivity did not recover to its initial value even at the lowest effective confining pressure. As stated above, H374 had a visible fracture, and its hydraulic conductivity was higher than those of other specimens.

3.4.3 Specific storage

Fig. 3.6 shows the specific storage of the specimen plotted under effective confining pressure conditions. Just like for the hydraulic conductivity results, for the differential flow rate condition measurements shown in Table 1, the results with the smallest error range (i.e., the most accurate) were used in the figure. For the case of low effective confining pressures, the specific storage error range had relatively large values. For example, with 8 MPa of effective confining pressure, all error ranges for specific storage were below $\pm 1 \times 10^{-5}$ m^{-1}. The specific storage in V291, H291 and H466 was observed to decrease with increasing effective confining pressure, although this tendency was not significant in comparison to the trends in hydraulic conductivity. Accordingly, no meaningful relationship could be drawn between the specific storage of specimens and the porosity measured by mercury intrusion porosimetry. After unloading, the specific storages of H223 and V291 increased about 4×10^{-5} m^{-1}; however, there were seldom fluctuations in the values regarding other specimens. Hydraulic conductivity values for H374, with its visible fracture, decreased with increasing effective confining pressure, while the specific storage was almost constant at all of the effective confining pressure conditions.

3.5 Discussion

3.5.1 Error evaluation of the hydraulic constants

The stress dependency of hydraulic constants for mudstone has been extensively reported (e.g., Tanikawa et al. 2008; Uehara et al. 2012; Kawamura et al. 2004; Zeng et al. 2014). Due to changes in hydraulic constants with effective confining pressure, which can be orders of magnitude in size, measurements of such changes at different pressures are of specific importance. In recent years, more attention has been given to the hysteresis observed in hydraulic constants and effective confining pressure of mudstones. Hydraulic conductivity decreases as pressure increases. Then, during the unloading process, there is almost no recovery in the mudstone permeability. Because the volumetric change with pressure in mudstone is related to consolidation history, hydraulic conductivity will not return to its initial value during unloading if the effective confining pressure is higher than that experienced during the rock's consolidation history. In the present study, these trends for hydraulic conductivity with accurate data and a small error range (Fig. 3.5) were observed. However, as the sensitivity of specific storage is less than that of hydraulic conductivity, the accuracy of the specific storage determination is generally poorer than that of hydraulic conductivity (Kato et al. 2013; Tokunaga and Kameya. 2003). The values of specific storage taken from *in-situ* experimental data are not useful for numerical simulation due to their low accuracy. In the laboratory experiment, Tokunaga and Kameya (2003) suggested that the ratio of the storage capacity of the apparatus to that of the specimen (δ') should be < 0.3 based on theoretical analysis and < 0.7 based on experimental results to obtain the specific storage in the specimen with sufficient accuracy. Storage capacity of the apparatus used in this study was 2.34×10^{-10} m^2, and δ' was found to be 0.3 for the specific storage for a specimen at 3.0×10^{-5} m^{-1} with a length of 25 mm and a diameter of 50 mm. When the value of specific storage of the specimen is $< 3.0\times10^{-5}$ m^{-1}, δ' is > 0.3. All of the values obtained for δ' were smaller than 0.7 (Table 1), satisfying the required accuracy from the experimental results.

Because the storage capacity of a mudstone with about 30% porosity is comparatively large, it was come to light that specific storage can be calculated accurately by the flow pump method.

There are two ways to minimize the error range in determinations of specific storage for the flow pump method. The first is using a bigger specimen to increase the specific capacity of specimen. However, it is difficult to make bigger specimens due to limitations regarding the pressure vessel volume, sampling core size and disturbance. The second is to increase the flow rate to raise the equilibrium pressure. Increasing the equilibrium pressure means the differential pressure is higher than pressure resolution of the assemblage and increasing measurement time in reaching a steady state in applying differential pressure. Comparing each pressure condition in the equilibrium state, note that the error range of the specific storage was reduced as the flow rate increased. There is one problem with increasing the flow rate—a larger differential pressure between the upstream end face of the specimen and its downstream end surface. The hydraulic head distribution of time-dependent change during the flow pump experiment, which was calculated using Eq. (7), is shown in Fig. 3.7. A specimen was divide into five equal sections that formed downstream end surfaces at 0.0 L, 0.2 L, 0.4 L, 0.6 L, 0.8 L, and 1.0 L in elevation (upstream end surface) where L is the length of each specimen. Fig. 3.7 also shows the pressure propagating from upstream to downstream end surfaces almost equally. When the equilibrium pressure was 100 kPa at a 25 mm specimen length, the differential pressure was suppressed at 4 kPa per 1 mm. This issue can possibly be attributed to the fact that the transient pressure damages specimens by deformation and/or clogging of fluid flow lines with clay particles, as these are common problems when using the transient pulse method. However, the differential pressure caused by the flow pump method gradually increased as time advanced. The flow rate was increased using the conventional flow pump method to improve the accuracy of specimen's specific storage determination. Hence there is no need to measure strain in the specimens, thereby leading to fewer time demanding procedures.

3.5.2 Evaluation of the specific storage

In an experiment that used the same mudstone that is examined in the current study, the transient pulse method determined that the specific storage ranged from 1.1×10^{-5} to 4.3×10^{-5} m^{-1} for effective confining pressures of 1 to 19 MPa (Kawamura et al. 2004). After excluding the data with the greatest errors, the measured values in this study fell to between 2.0×10^{-5} and 6.0×10^{-5} m^{-1}, in agreement with previous work. Hence it was concluded that the specific storage of the specimen was related to the porosity, as increasing the effective confining pressure generally causes a reduction in porosity and specific storage. Previous studies based on calculations related to porosity changes with pressure in mudstone suggest that the specific storage of a sample decreases as the effective confining pressure increases (Tanikawa et al. 2008). The results of specific storage results for samples V291, H291 and H466 also showed slight decreases with increasing effective confining pressure (Fig. 3.6). The trend of decreasing specific storage with increasing effective confining pressure conforms to the theory of poroelasticity. The specific storage of a porous medium can be determined to be (Tokunaga et al. 2001)

$$S' = \frac{\rho_f g \alpha}{KB}, (16)$$

in which ρ_f is the density of the pore fluid, g is the gravitational acceleration, α is the Biot–Willis parameter, K is the bulk modulus at the drained states and B is Skempton's B coefficient. The values of K and effective confining pressure have a positive correlation. It is generally true that decreasing specific storage corresponds to increasing effective confining pressure. In the cases of samples H223 and H374, however, the values of specific storage at low effective confining pressures (2–3 MPa) are lower than that at high effective confining pressures (4–8 MPa). It is likely that these problems resulted from the stiffness of the heat shrinkable jacketing tube as opposed to the elasticity of mudstones and/or small temperature

fluctuation during the experiment. One way to improve the measurement of hydraulic constants is by using a soft jacket such as silicone lubber, thereby preventing seepage between the specimen and heat shrinkable tube. In addition, this error range can be minimized by considering the value of the flow rate.

3.6 Conclusions

The one of purpose of this study was to evaluate the hydraulic constants of sedimentary rocks including error using the flow pump method, a technique that is generally thought to be able to handle wider ranges than the transient pulse method. In this chapter, background information was considered that set the stage for the theoretical analysis for calculating hydraulic constants and evaluating error ranges based on the nonlinear least-squares method. Following that, flow pump experiments for the Horonobe mudstone were conducted with the effective confining pressure gradually increasing from 2 to 10 or 12 MPa, with subsequent unloading to the initial value. The hydraulic conductivity was observed in all cases to decrease with increasing effective pressure in the specimens, and after unloading, the hydraulic conductivity did not recover to its initial value. Generally, specific storage decreased with increasing effective confining pressure, although this tendency was not significant when compared to the similar trend for hydraulic conductivity. The error range in specific storage determinations was observed to be reduced at higher flow rates considering the similar condition for pressure. The analytical results show that the pressure distributed almost equally from the upstream to downstream end surfaces and that the differential pressure developed by the flow pump method gradually increases as time advances. The ratio of the storage capacity of the apparatus to that of the specimen (δ') should be < 0.3 for theoretical analysis and < 0.7 for experimental results to obtain a sufficiently accurate specific storage in the specimen. All of δ' values that the results of this study obtained were < 0.7,

which showed sufficient accuracy in the experimental results. Because the storage capacity of a mudstone with about 30% porosity is comparatively large, it was determined the specific storage can be calculated accurately by the flow pump method. At an effective confining pressure of 8 MPa, the error ranges for the specific storage were all below $\pm 1 \times 10^{-5}$ m^{-1}, which supports the higher reliability of the flow pump method for assessments of specific storage in mudstone.

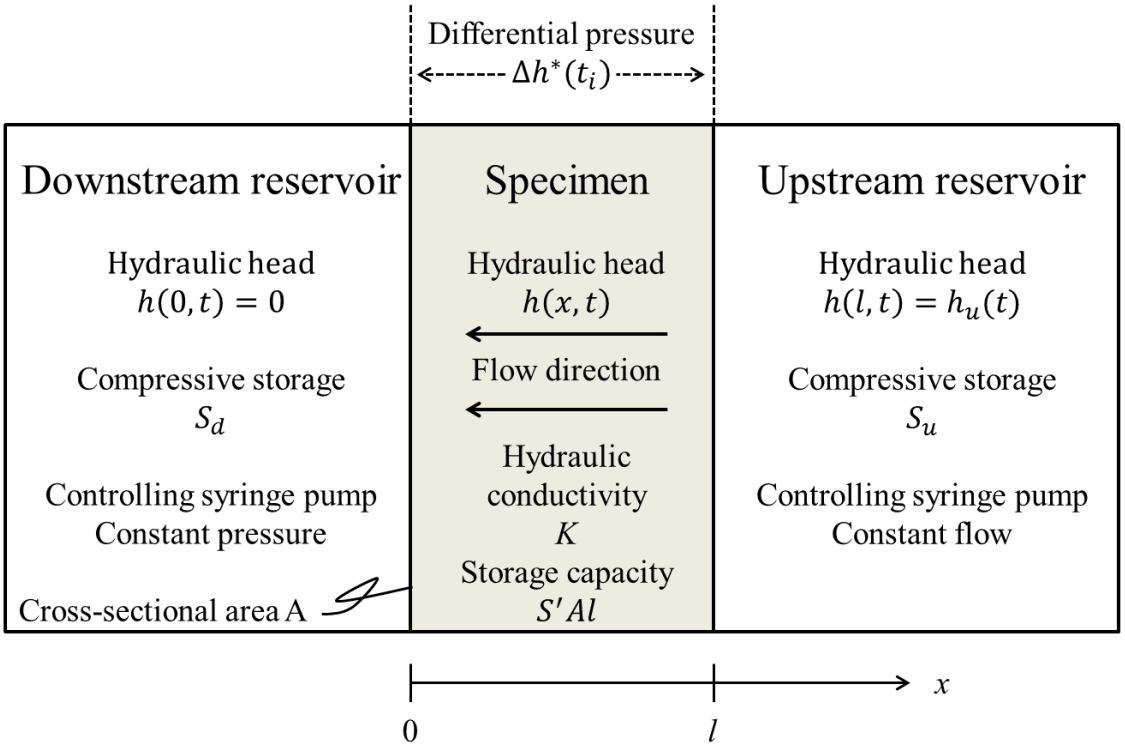

Fig. 3.1 Schematic diagram and the boundary conditions associated with the flow pump method

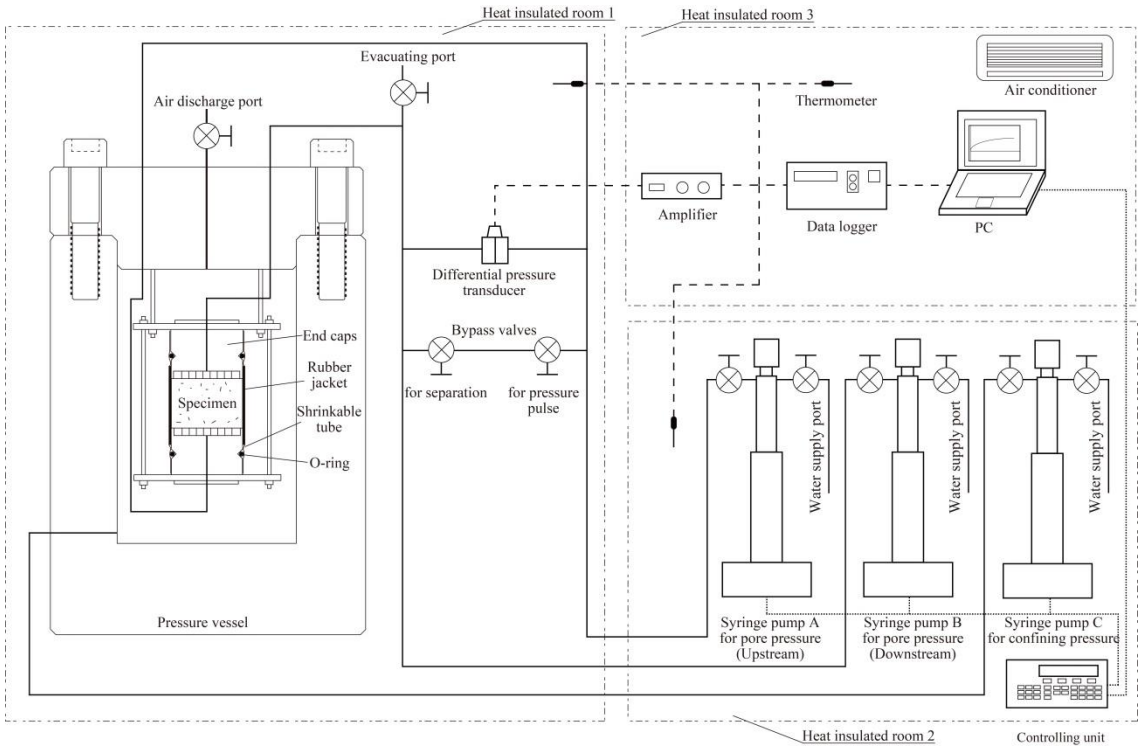

Fig. 3.2 Schematic diagram of apparatus for measurements of hydraulic constants

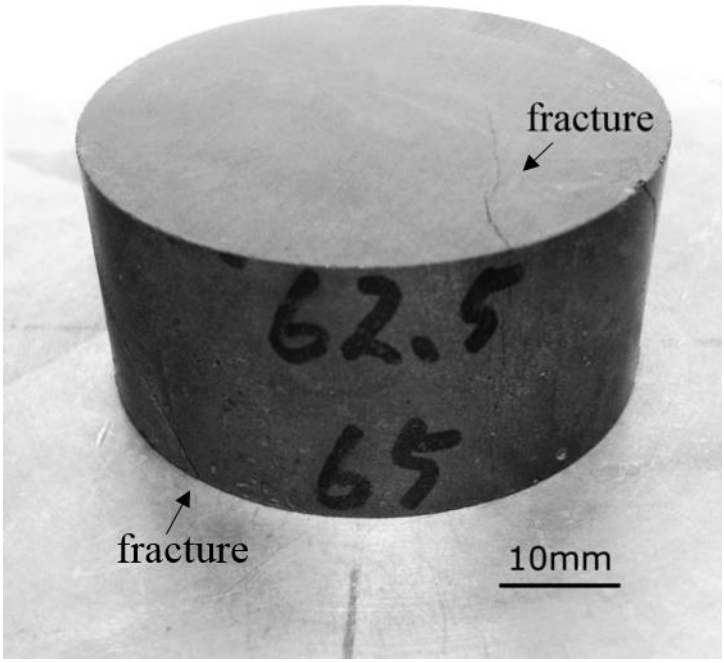

Fig. 3.3 Photograph of specimen H374. Visible fractures are seen in the specimen. Nevertheless it is considered independent. Labels 62.5 and 65 mean that this specimen was cored from 374.625–374.650 m.

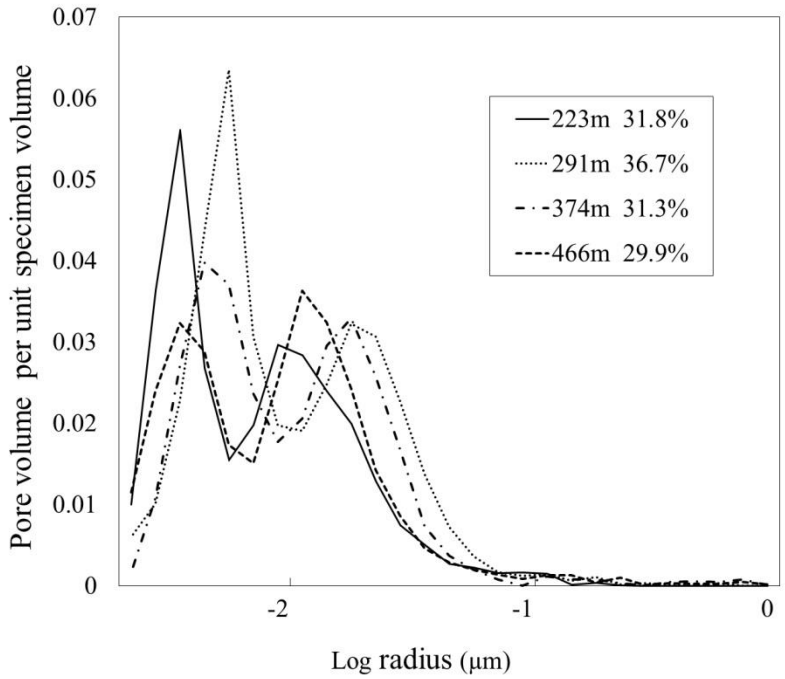

Fig. 3.4 Total porosity and pore size distribution of mudstones with mercury intrusion porosimetry.

Table 3.1 Experimental results of HDB4-H374 under a different flow rate conditions.

effective confining pressure (MPa)	flow rate Q(μl/min)	equilibrium pressure (kPa)	hydraulic conductivity *K*(m/s)	error range of *K* (m/s)	Specific storage *S'*(1/m)	error range of *S'* (1/m)	ratio of the storage capacity δ'
2	50	26.0	3.89×10^{-9}	1.70×10^{-10}	2.94×10^{-5}	2.63×10^{-5}	0.32
2	100	52.8	3.82×10^{-9}	1.20×10^{-10}	2.17×10^{-5}	2.02×10^{-5}	0.44
2	150	82.4	3.68×10^{-9}	1.06×10^{-10}	1.62×10^{-5}	1.98×10^{-5}	0.59
4	10	24.8	8.13×10^{-10}	4.48×10^{-11}	2.38×10^{-5}	1.41×10^{-5}	0.40
4	20	50.2	8.05×10^{-10}	2.84×10^{-11}	2.55×10^{-5}	1.05×10^{-5}	0.37
4	30	76.4	7.93×10^{-10}	1.97×10^{-11}	2.41×10^{-5}	8.79×10^{-6}	0.38
6	5	41.4	2.44×10^{-10}	1.52×10^{-11}	2.46×10^{-5}	1.06×10^{-5}	0.39
6	10	78.5	2.57×10^{-10}	1.14×10^{-11}	2.96×10^{-5}	9.24×10^{-6}	0.32
6	11	90.7	2.45×10^{-10}	6.33×10^{-12}	2.54×10^{-5}	5.18×10^{-6}	0.40
8	2	56.1	7.20×10^{-11}	2.95×10^{-12}	2.61×10^{-5}	7.78×10^{-6}	0.36
8	3	87.2	6.95×10^{-11}	1.86×10^{-12}	2.74×10^{-5}	6.84×10^{-6}	0.35
6	2	53.2	7.58×10^{-11}	4.53×10^{-12}	3.10×10^{-5}	1.13×10^{-5}	0.31
6	3	79.9	7.58×10^{-11}	2.31×10^{-12}	3.32×10^{-5}	9.17×10^{-6}	0.29
4	1	26.5	7.61×10^{-11}	8.36×10^{-12}	3.23×10^{-5}	1.99×10^{-5}	0.29
4	2	50.5	8.00×10^{-11}	3.48×10^{-12}	2.56×10^{-5}	1.03×10^{-5}	0.37
4	3	77.1	7.86×10^{-11}	1.89×10^{-12}	2.66×10^{-5}	6.88×10^{-6}	0.36

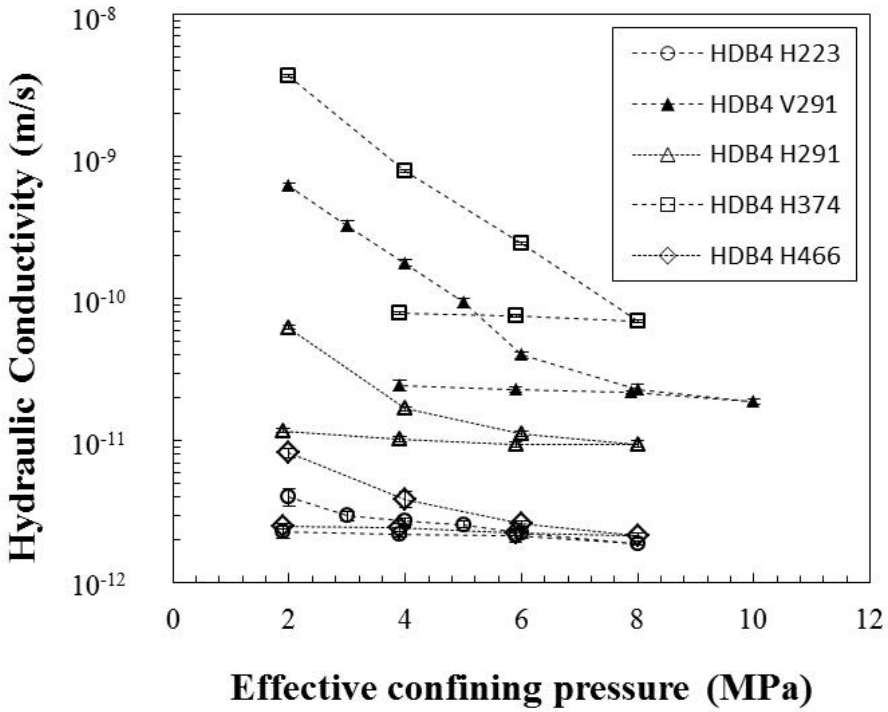

Fig. 3.5 Hydraulic conductivity for specimens versus effective confining pressure.

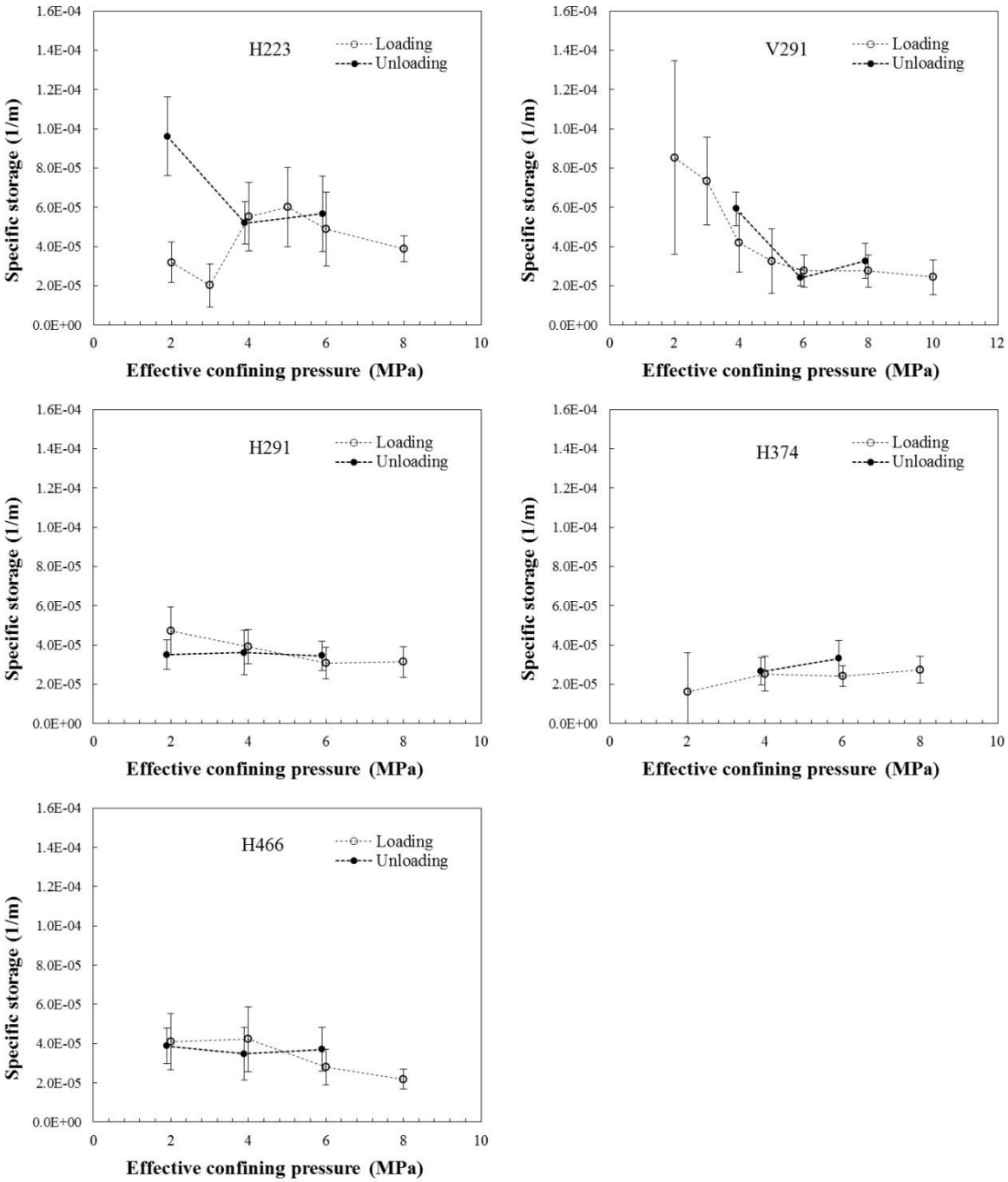

Fig. 3.6 Specific storage for specimens versus effective confining pressure.

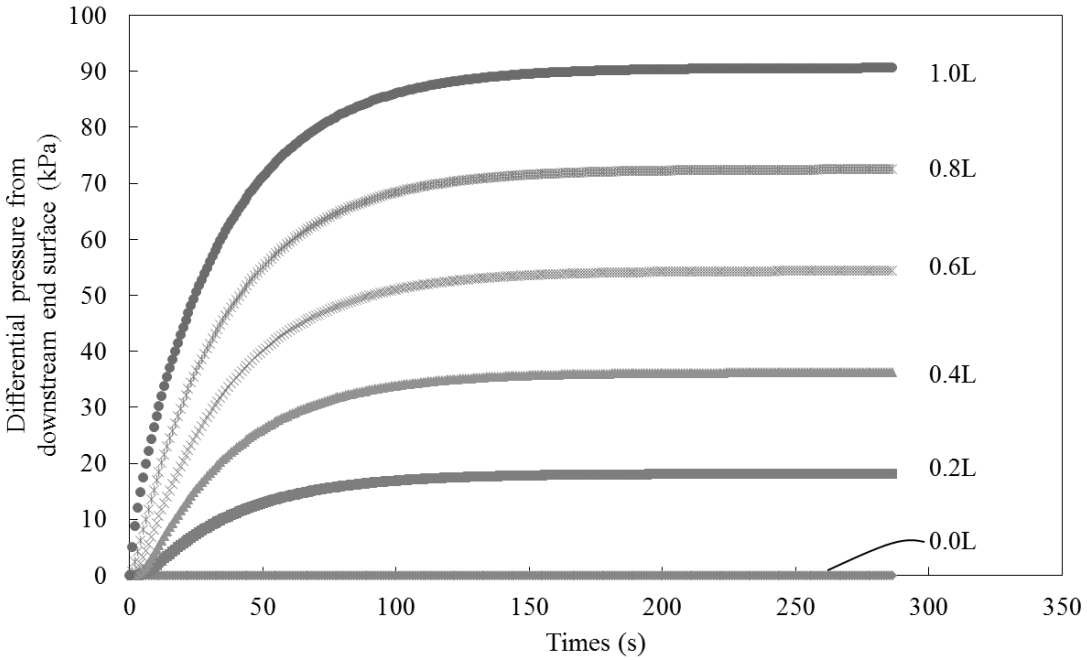

Fig. 3.7 Hydraulic head distribution of time-dependent change during the flow pump experiment. The specimen was analytically divided into five equal sections which are determined to from downstream end surface 0.0 L to 0.2 L, 0.4 L, 0.6 L, 0.8 L, 1.0 L (upstream end surface) where L is the length of each specimen.

4. Development of the permeability anisotropy of some sedimentary rocks under true triaxial stresses

4.1 Introduction

Some researchers conducted permeability experiments during conventional triaxial compression ($\sigma_3=\sigma_2<\sigma_1$) and extension ($\sigma_3<\sigma_2=\sigma_1$) using the cylindrical specimen for weakly-cemented sandstone (Zoback and Byerlee. 1976; Bruno. 1994), or porous sandstone including Berea sandstone Zhu et al. (1997; 2002). Recent efforts focused on permeability change during deformation has also been described by improving experimental methods under conventional triaxial compression experiments such as permeability measurements during cyclic loading conditions for investigating cumulative damage and permeability hysteresis of granodiorite and Westerly granite (Mitchell and Faulkner, 2008) or hydro-mechanical coupling during compressive deformation and development of damage zone of granite (Chen et al. 2014), measurements of permeability and structural changes of several kinds of rocks (welded tuff, sandstone and granite) using thin section analysis and X-ray CT tomography (Alam et al. 2014), permeability measurements of fault gouge in mudstone (Uehara and Takahashi. 2014). However, these conventional triaxial compression methods have some limitations due to cylindrical geometry of specimen: uni-axial compression or extension must be applied under the isotropic confining pressure. In addition, because only the upper and lower ends of the specimen being attached to the end-pieces, the permeability measurement is limited to only the vertical direction. Fracturing at a low angle to the maximum principal stress (σ_1) is eventually occured by increasing axial stress. However, conventional triaxial testing using cylindrical specimens is unable to measure accurate permeability values parallel or perpendicular to the fracture. Conversely, the true triaxial experiment that uses rectangular prismatic specimens enables to measure permeability accurately parallel to the final fracture that is parallel to the intermediate principal stress (σ_2)

direction (Mogi, 1971a). Since the 1970s, researchers became aware through true triaxial testing (Mogi, 1971a, b; King, 2002; Takahashi, 2012) that the σ_2 has a large control on the fracture strength, mechanical behavior, crack distribution and permeability anisotropy of the deformed rocks. Thus, understanding the effect of the stress ratio on the development of permeability anisotropy is crucial.

Some studies have been conducted on the permeability measurements of the σ_2 direction under true triaxial conditions using rectangular prismatic specimens. Li et al. (2002) and Takahashi et al. (1993 and 2004) investigated the permeability of the σ_2 direction for Shirahama sandstone using Mogi-type true triaxial test apparatus (Mogi, 1971a,b). Li et al. (2002) determined that the permeability in the σ_2 direction decreased with increasing σ_1 and σ_2 before yield stress. Takahashi et al. (2004) showed that the permeability after the failure increased at low confining pressure (i.e. 8 MPa). Conversely, at a higher confining pressure (i.e. 63 MPa) in a ductile regime, the permeability after the failure was less than the initial value. These methods allow the measurement of the permeability along the σ_2 direction; however, no previous study has measured the σ_1 and σ_2 directions simultaneously using Mogi-type true triaxial test apparatus. This study aimed to evaluate how the stress ratio affects the permeability anisotropy. For this purpose, the flow pump method has been incorporated and permeability measurement lines in the direction of σ_1 were added for the permeability anisotropy measurement into an upgraded Mogi-type true triaxial test apparatus (Takahashi et al. 2004). Using this apparatus, experiments were conducted on Berea sandstone and Amatsu mudstone.

4.2 Experimental procedure

4.2.1 Experimental equipment

The tests were conducted using the Mogi-type true triaxial test apparatus of the National

Institute of Advanced Industrial Science and Technology of Japan. In this apparatus, maximum and intermediate stresses are applied through two pairs of rigid pistons and minimum stress directly by oil pressure. The servo-controlled apparatus enables three principal compressive stresses to be applied independently. Three loading axes were assigned as follows: the X axis is the horizontal σ_3 direction, the Y axis is the horizontal σ_2 direction, and the Z axis is the axial σ_1 direction. Fig. 4.1 shows the schematic drawing of the permeability test system under true triaxial stress conditions. The specimen (1) was jacketed with silicone rubber (9). The porous metals (4) of the Y direction have 66 holes, and a copper foil was placed between the porous metals (4) and the end-pieces (2). Metal meshes (5) were placed between the specimen (1) and the end-pieces of the Z direction (3). Three local deformation transducers (LDT) (6, 7, 8) were used to measure the deformation of the specimen. In the Z and Y directions, each upstream and downstream line was connected to an ISCO syringe pump (a) and (b), respectively. The permeability was measured using a flow pump. Li et al. (2002) used a transient pulse method to shorten the experimental time; however, this method cannot be used for high permeability specimens such as Berea sandstone. A wide range of permeability (10^{-21} to 10^{-11} m^2) can be measured using the flow pump method (Olsen. 1966; Lin et al. 2003). Therefore, this method was adopted to ease the response to permeability changes caused by deformation during the experiments. In this method, the permeability of a saturated specimen is estimated by measuring the induced flow rates under a constant hydraulic gradient. A rigorous solution to the flow pump method that account for the storage capacities of the specimen as well as equipment was developed by the previous works (Morin and Olsen, 1987; Esaki et al. 1996; Zhang et al. 2002). The permeability of specimens were calculated using this method. The storage capacity of the system was calculated in advance using a dummy specimen made of brass.

4.2.2 Specimen description

The specimens used were rectangular prismatic blocks with dimensions of 70 mm × 35 mm × 35 mm and surface parallelism was ±50μm. The specimens were prepared to have the longer sides perpendicular to the bedding planes. The selected rocks were Berea sandstone (USA) and Amatsu mudstone (Boso Peninsula, Japan). The Berea sandstone was chosen as a control because there are numerous previous reports on various mechanical behavior and/or permeability. Thus, by comparing the results of this study and previous studies it is possible to assess the reliability of measurement. The mechanical behavior and permeability of the Amatsu mudstone is unknown. Similar rocks to Amatsu mudstones are widely distributed in the Boso peninsula in an arc-arc collision zone, and such mudstones are thought to have important controls on deformation of whole sequence to form an accretionary prism. The permeability of mudstone is important in the subsurface stress environment because mudstone has a large changeable permeability due to pore collapse or flow/failure caused by compressional or extensional stress. Before conducting the experiments, the porosity was measured of Berea sandstone to be 19.5%, and that of Amatsu mudstone to be 40% using a mercury intrusion porosimetry.

4.2.3 Test procedure

This study focused on investigating the effect of σ_2 and permeability anisotropy development. Therefore, σ_3 was kept constant at 10 MPa for the Berea sandstone and 3 MPa for the Amatsu mudstone after initial isotropic loading. The pore pressure was also kept constant at 1 MPa after the initial loading. In the experiment described herein, the three principal stresses were applied in the following order, as shown in Fig. 4.2. First, the hydrostatic pressure was applied to the minimum principal stress value A (σ_3). Second, loads along the Y and Z axes were increased simultaneously by load control to the intermediate principal stress value B (σ_2).

Third, load along the Z axis was increased by stroke control to the final strength C (σ_1). For the Berea sandstones, further investigation was conducted where σ_1 and σ_2 are both increased to reach σ_2 higher values. During the above processes, permeability measurement was conducted as necessary during temporary pauses in loading. These procedures for permeability measurement under true triaxial conditions are illustrated in Fig. 4.3.

4.3 Experimental results

The values of permeability under the different stress conditions are summarized in Table 1. Axial strains ε_x, ε_y, and ε_z were defined as the three principal strains about the X, Y, and Z axes. ε_v denotes volumetric strain. Fig. 4.4 shows the examples of experimental results of Berea sandstone and Amatsu mudstone at a constant pore pressure (1 MPa). Fig.4.4a is a plot for the Berea sandstone of the differential stress against the strain during the experiment with confining pressures σ_3 maintained at 10MPa and σ_2 maintained at 21.4MPa (run BSS2 in the Table 1). The first and second permeability measurement was conducted at a hydrostatic pressure of 10 MPa, and at increased biaxial stresses where σ_1=σ_2=21.4 MPa. Three more permeability measurements were conducted while σ_1 was increased to 124.6 MPa just before the failure at 132.6 MPa. Post failure permeability was also measured after the stress drop at a static condition. Fig. 4.4b is a plot for the Amatsu mudstone with run Am-m2 experimental condition in the Table 1. The first and second permeability measurement was conducted at a hydrostatic confining pressure (σ_3) that was maintained at 3 MPa throughout the later processes, and at increased biaxial stresses where σ_1=σ_2=10.0 MPa. The third permeability measurement was conducted while σ_1 was increased to 14.0 MPa while σ_2 maintained at 10.0MPa. The fourth permeability measurement was conducted after the peak stress. The stress drop for the Amatsu sandstone was not clear comparing with the Berea sandstone. The sudden stress reductions of the Amatsu mudstone after the peak stress are the influence of stress relaxation while the loading was stopped for the forth permeability measurement. After

the load of Z direction was increased to the 1% axial strain of Z direction (ε_z) from peak stress, the fifth permeability was measured as a post failure permeability.

4.3.1 Mechanical properties

Fig. 4.5 shows strength of the test piece σ_1 plotted against σ_2 at the failure under a constant confining pressure σ_3. The σ_1 at the failure increased as σ_2 become higher until it reached to a peak or plateau for the Berea sandstone (Fig. 4.5a). A gradual decline of σ_1 follows at higher σ_2 conditions after the peak. This tendency was similar to those observed in previous studies (Mogi. 1971a; Chang and Haimson. 2000; Haimson and Chang. 2002; Oku et al. 2007; Haimson & Rudnicki. 2010). For the Amatsu mudstone, this tendency was unclear due to the limited number of the experiment.

The shape of the stress is described here by the Nadai–Lode parameter μ_σ:

$$\mu_\sigma = 2\left(\frac{\sigma_2^{peak} - \sigma_3^{peak}}{\sigma_1^{peak} - \sigma_3^{peak}}\right) - 1$$

The μ_σ is also referred to intermediate principal stress ratio. The stress state $\mu_\sigma = -1$ implies uniaxial compressional stress ($\sigma_1>\sigma_2=\sigma_3$), and the stress state $\mu_\sigma = 1$ uniaxial tensional stress ($\sigma_1=\sigma_2>\sigma_3$): these stress regimes are achieved by conventional triaxial compression testing, and conventional triaxial extension or reduced triaxial extension testing, respectively. $\mu_\sigma = 0$ implies that $\sigma_2 = (\sigma_1+\sigma_3)/2$ and a plane stress. True triaxial compression machine enables to measure permeability behaviors under $1>\mu_\sigma>-1$ stress conditions without discontinuity. Fig. 4.6 shows a plot of μ_σ against ε_v^{pf} volumetric strain after the failure and the stress drop. The value of ε_v^{pf} of the Berea sandstone is the end-point of ε_v in Fig. 4.4a. If ε_v^{pf} is negative, the bulk volume of the specimen after the failure is larger than that at the initial hydrostatic condition. In the case of the Berea sandstone, $\varepsilon_v^{pf} = -0.14\text{x}10^{-2}$ at the intermediate principal stress ratio $\mu_\sigma = -0.79$. As μ_σ increase, the ε_v^{pf} increases and becomes positive (volume decreases comparing with the initial state). At μ_σ=0.16, Berea sandstone shows the highest ε_v^{pf}

value ($1.12x10^{-2}$). At μ_σ=0.62, the ε_v^{pf} decreased to $0.66x10^{-2}$.

In case of the Amatsu mudstone, the stress drop was not clear (Fig. 4.4b). The post failure volumetric strain ε_v^{pf} of the Amatsu mudstone was taken at the point where the axial strain of Z direction (ε_z) increased by 1% from the axial strain at the peak stress. ε_v^{pf} of the Amatsu mudstone was the highest at μ_σ=−0.06 (Fig. 4.6b). The compressibility of the both Berea sandstone and Amatsu mudstone became the highest around μ_σ = 0.

Fig. 4.7 shows microfocus X-ray computed tomography (CT) images of the Berea sandstone after experiments under different σ_2 conditions. Shear fractures were present at μ_σ =−0.62 and nearly vertical shear fractures were observed at μ_σ = 0.62. As the underlying assumption of the Mohr failure criterion, fault angle θ (angle between fault and horizontal direction) gradually decreases as the confining pressure rises. True triaxial tests, however, demonstrate that fault angle is varied not only as a function of σ_3, but also as a function of σ_2 for the same σ_3. Commonly, θ rises with increase in σ_2 (Chang & Haimson, 2000; Oku et al. 2007; Haimson & Rudnicki. 2010). The results of fault angle at μ_σ = −0.62 was 61°, but at μ_σ = 0.62, 77°to 83°. Fig. 4.8 shows CT images of the Amatsu mudstone after experiments under different σ_2 conditions. Conjugate fractures were present at μ_σ =−0.37 and shear fractures were obserbed at μ_σ =−0.06. Fig. 4.8 shows fractures with a density lower than the surrounding rock mass. Therefore, it is probable that high permeability to σ_2 direction with stress release of the deformed rock after unloading condition.

Fig. 4.9 illustrates the photomicrographs of polished thin sections of the Berea sandstone perpendicular to the Y direction after the experiment. Dark area corresponds to pore spaces. The direction of shear movement is marked by arrows along the fault. At the μ_σ=−0.81 condition (Fig. 4.9a), the shear fracture exhibits almost no evidence for cataclasis. At the μ_σ= −0.62 and −0.44 conditions (Fig. 4.9b, c), cataclastic deformations (microcracks with cataclasis) were observed around the fault planes. Furthermore, at the μ_σ =−0.44 condition (Fig. 4.9c), a preferred orientation was observed in microcracks that aligned parallel to the Z

direction. For the $\mu_\sigma > 0$ condition (Fig. 4.9d, e, f), a set of gouge layer was formed parallel to the fault plane that accompanied pore collapse around the fault plane. At the $\mu_\sigma = 0.16$ condition (Fig. 4.9e), conjugate fractures occurred. For the $\mu_\sigma = 0.68$ condition (Fig. 4.9f), fracture plane was almost parallel to the Z direction.

4.3.2 Permeability properties

Figs. 4.10 and 4.11 are plots of normalized permeability $\log_{10}(k/k^0)$ against mean stress σ_m for the Berea sandstone and Amatsu mudstone respectively, where k^0 is the values of initial permeability under hydrostatic confining pressure. The mean stress σ_m is defined as

$$\sigma_m = (\sigma_1 + \sigma_2 + \sigma_3)/3$$

In these figures, the normalized permeability along Z-axis and Y-axis are shown separately in (a) and (b). Open symbols are the post-failure data.

The obtained permeability at hydrostatic conditions coincide with previous reports that measured permeability along Z-axis using conventional triaxial apparatus (Zhu et al. 1997, 2002). The permeability of the Berea sandstone in the Z direction (Fig. 4.10a) indicates that under $\mu_\sigma = -0.79$ condition, the permeability was almost unchanged with increasing σ_m. When $\mu_\sigma > -0.62$, the permeability decrease with increasing σ_m. There was a rapid permeability reduction at a high pressure beyond $\sigma_m = 80$ MPa. In contrast, the diminution of Y direction permeability (Fig. 4.10b) was less than the Z direction permeability. The post-failure permeability of the Berea sandstone in the Z direction decreased dramatically and became about one order magnitude smaller than that in the Y direction under the positive μ_σ conditions. For the Amatsu mudstone, the permeability in the Y and Z directions both decreased with increasing σ_m keeping almost the same pace (Fig. 4.11a, b). Thus, the development of the permeability anisotropy with increasing stresses was more pronounced in the Berea sandstone than the Amatsu mudstone.

4.4 Discussion

4.4.1 Influence of intermediate principal stress ratio (μ_σ) on mechanical behavior

Fig. 4.5 shows that the σ_1 value at the failure increased with elevated σ_2 until it reached to a plateau. Similar trends have been generally observed in other true triaxial compression experiments under an asymmetric homogeneous triaxial state of compressive stress on different rock types such as dolomite and limestone (Mogi. 1971a), amphibolite (Chang and Haimson 2000), Westerly granite (Haimson & Chang. 2000; Takahashi et al. 2012) and tuffaceous sandstone (Takahashi et al. 2014). Chang and Haimson. (2000) also revealed the subparallel alignment of microcracks deformed under high μ_σ condition are more prominent than that of low μ_σ condition. In general, $\sigma_X = \sigma_Y$ condition on conventional compression experiments, the strain of the horizontal direction shows $\varepsilon_X = \varepsilon_Y$ dilatation identically. In the case of $\sigma_X < \sigma_Y$ condition on true triaxial experiments using rectangular prismatic specimen, however, the dilatation of Y direction is smaller than that of X direction. The results showed $\varepsilon_X < \varepsilon_Y$ in the Fig. 4.4 experimented under $\sigma_X < \sigma_Y$ conditions. Accordingly, opening microcracks perpendicular Y direction during loading σ_Z are confined by higher μ_σ conditions. Under different μ_σ conditions, the changing fracture patterns after failure was also observed in Fig. 4.7.

Development of microcracks during true-triaxial stresses was examined by means of anisotropy of seismic wave velocity (Takahashi et al. 2012). The effect of stress induced microcracks to the velocity is described by a simple parameter (O'Connel and Budiansky, 1974):

$$N\langle a^3 \rangle = \frac{3}{4\pi} \frac{\phi}{\langle \alpha \rangle}$$

when very thin spheroidal or ellipsoidal dry cracks are randomly distributed in the solid. $\langle \alpha \rangle$ denotes the mean major axis of the ellipsoid, N is the number of cracks per unit volume of the solid, ϕ is the volume of cracks per unit volume of the solid:

$$\phi = \frac{4}{3}\pi \langle a^2 c \rangle \mathrm{N}$$

Parameter and α is the aspect ratio of the spheroidal cracks (c/a). According to Soga et al. (1978), velocities in three orthogonal directions can be well described using the crack density parameter defined by O'Connel and Budiansky (1974). Using Soga's equations (Soga et al. 1978), Takahashi et al. (2012) calculated crack densities and average aspect ratios of flat spheroidal cracks. Their calculation required presence of cracks using with two different orientations that are perpendicular to the σ_X and σ_Y directions at low σ_Y conditions. At higher σ_Y conditions, the density of cracks perpendicular to the σ_Y direction was significantly reduced and the cracks perpendicular to the σ_X direction became predominant (Takahashi et al. 2012; 2014). Fig. 4.12 shows the summary of microcrack distribution and final fracture comparing the $\mu_\sigma = -1$ and 1 conditions from the results and referring to previous works of SEM micrograph observation (Chang and Haimson. 2000) and seismic wave analysis for microcrack propagation (Takahashi et al. 2012). As microcrack propagation during loading are changed depending on μ_σ, it is assumed that the permeability of the specimen is also affected by μ_σ. This is examined further in the following chapter.

4.4.2 Permeability anisotropy

Permeability reduction were observed with increasing mean stress for all the specimens with the exception of the Z direction of BSS2 at $\mu_\sigma = -0.79$ condition (Table 1). Fig. 4.13 shows the normalized permeability $\log_{10}(k^{pf}/k_0)$ versus the stress ratio μ_σ. Normalization of the parameter ($\log_{10}(k^{pf}/k_0)$) is based on their permeability at hydraulic stress. k_0 is the permeability at hydrostatic stress before the increment of the sigma2. In the $\mu_\sigma < 0$ condition, the permeability of both directions (k_Z^{pf} and k_Y^{pf}) showed approximately the same decrease compared with the initial value k_0. Conversely, under the $\mu_\sigma > 0$ condition, k_Z^{pf} of the Berea sandstone decreased more than k_Y^{pf}. It can be observed that the permeability anisotropy of the Z and Y directions appears to correlate with the comminution of grains (Fig. 4.9). The fluid in

the Z direction must flows through the pore-collapsed gouge layer; in contrast, because the Y direction is parallel to the gouge layer, fluid flow occurs through the pore spaces around the gouge layer. Thus, the formation of the gouge layer associated with increasing μ_σ caused permeability anisotropy in the Y and Z directions. Previous field research has suggested that permeability within natural fault zones and shear bands is anisotropic (Antonellini and Aydin, 1994; Shipton et al. 2002, 2005). Shipton et al. (2005) demonstrated that the permeability reduction was caused by reduced grain size and reduced pore-throat sizes. These field observations are in agreement with laboratory data (Zhang and Tullis, 1998). They measured permeability in synthetic quartz gouge produced by a rotary shearing at an effective confining pressure of 21 MPa. They observed that the permeability dropped by two to three orders of magnitude and that a permeability anisotropy of one order of magnitude difference was developed. The results of this study showed that k_Y^{pf} was slightly more than one order of magnitude larger than k_Z^{pf}.

Beyond the failure, the permeability data of conventional compression experiments and conventional extension experiments for the cylindrical specimens of Berea sandstone (Zhu et al. 1997) indicated that k_Z^{pf} exceeded k_X^{pf}. Menéndez et al. (1996) observed significant anisotropy in microcracking, which was evident in deformed specimens. The density of microcracks aligned parallel to σ_1 was about twice that of cracks parallel to σ_3 (Menéndez et al. 1996). It is unable to compare directly the results of permeability anisotropy (k_Z vs k_X) of Zhu et al. (1997) and the results of this study (k_Z vs k_Y). Clear permeability anisotropy was not observed in either Berea sandstone or Amatsu mudstone under low μ_σ conditions. If combining with the results of this thesis and Zhu et al. (1997, 2002), the permeability of σ_1 direction and σ_2 direction is the same and minimum permeability of σ_3 direction deformed at low μ_σ condition. Fig. 4.12 shows that the crack density of the plane perpendicular to the Y direction was markedly reduced under high μ_σ conditions. Accordingly, it is probable that the alignment of microcracks causes permeability anisotropy $k_Z > k_X$.

Experimental data were obtained on permeability reduction with increasing mean stress and development of permeability anisotropy correlated with the intermediate principal stress ratio in the Berea sandstone.

4.5 Conclusion

Berea sandstone and Amatsu mudstone were tested to measure the permeability anisotropy of the Z (σ_1) and Y (σ_2) directions under true triaxial compression conditions. The experimental technique was developed by incorporating a flow pump method into a Mogi-type true triaxial apparatus upgraded from Li et al. (2002) and Takahashi et al. (2004). This experimental setup allowed the measurement of permeability over the full process from elastic deformation to eventual faulting. Using this technique, this study evaluated how the stress ratio affected the development of the permeability anisotropy. Experimental data were obtained demonstrating permeability reduction with increasing mean stress and the development of permeability anisotropy correlated with the intermediate principal stress ratio (μ_σ) at the Berea sandstone. In conditions of lower μ_σ, the permeability of post-failure specimens decreased compared to the initial permeability. In contrast, in the $\mu_\sigma > 0$ condition, the permeability of the σ_1 direction decreased more than the permeability of the σ_2 direction. The micrographs of the polished sections of post-failure Berea sandstone show remarkable alignment of microcracks aligned parallel to the σ_1 direction and the generation of a gouge layer in the $\mu_\sigma > 0$ condition. The results suggest that σ_2 controls the mechanical behavior and crack distribution of deformed rocks under constant σ_3 conditions. Accordingly, the higher μ_σ condition induced the permeability anisotropy of Berea sandstones. In the Amatsu mudstone, there were also illustrated the permeability reduction with increasing mean stress however, the permeability anisotropy was observed. The results obtained from this study draw demonstrate to the importance of the experimental studies using true triaxial apparatus to determine the

permeability properties of rocks.

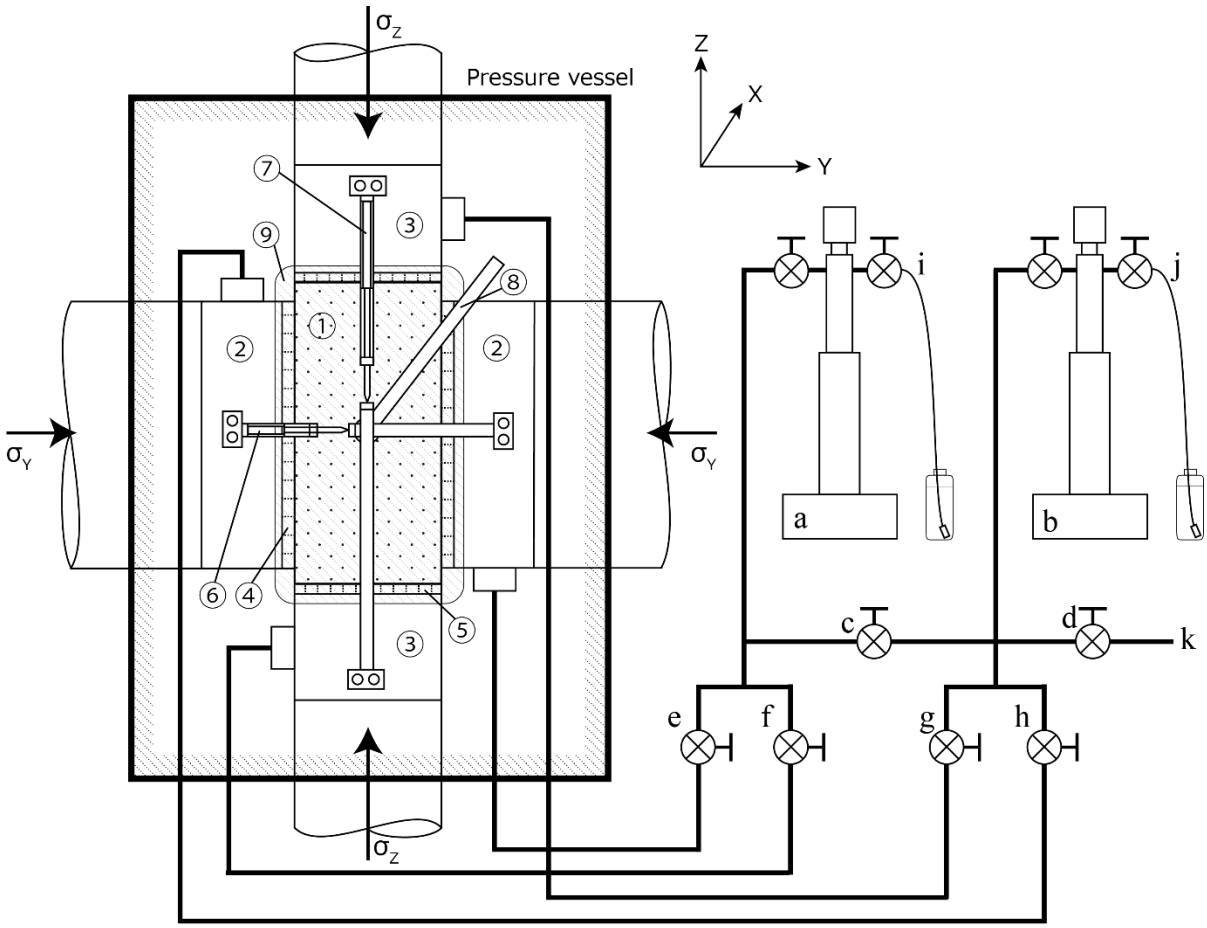

Fig. 4.1 Schematic diagram of the true triaxial apparatus and its assembly. 1: Specimen, 2 and 3: End-pieces of the σ_Y and σ_Z directions, respectively, 4: Porous metals, 5: Metal meshes, 6, 7, and 8: LDT for σ_Y, σ_Z, and σ_X, respectively, 9: Silicon rubber.

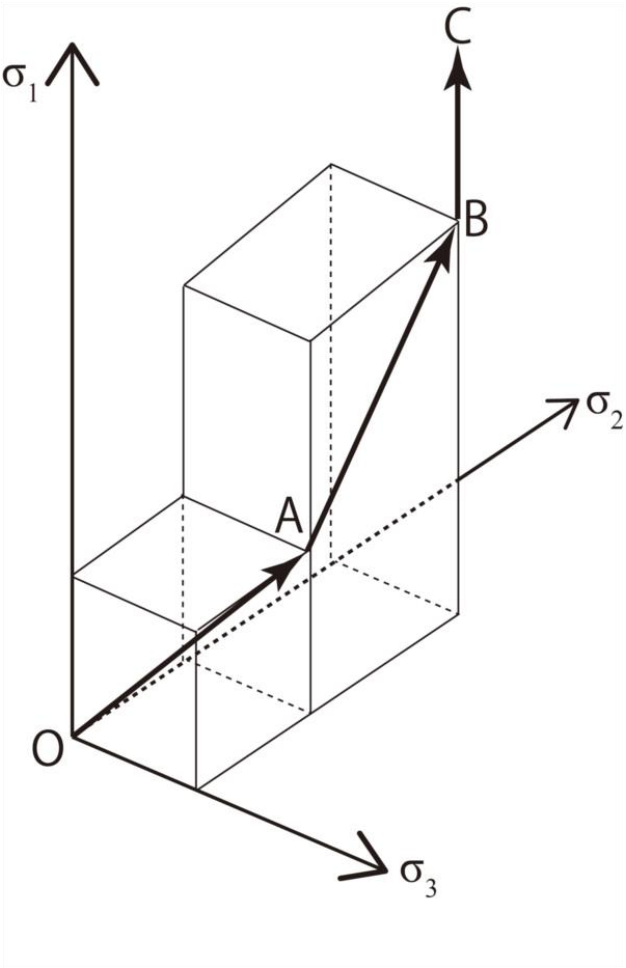

Fig. 4.2 Loading path of the principal stresses during the experiment.

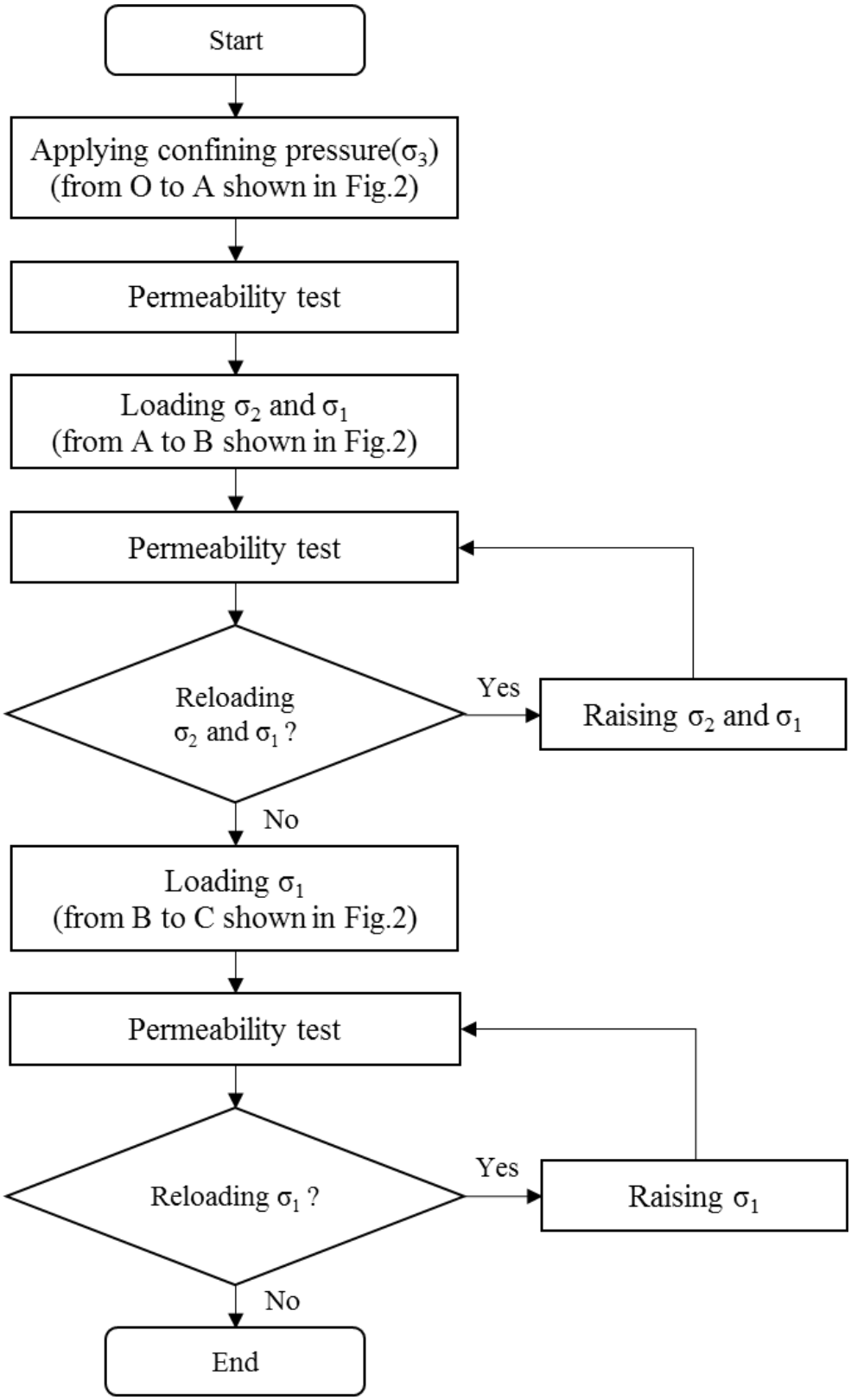

Fig. 4.3 Flow chart for the experimental procedure of permeability measurement under true triaxial conditions.

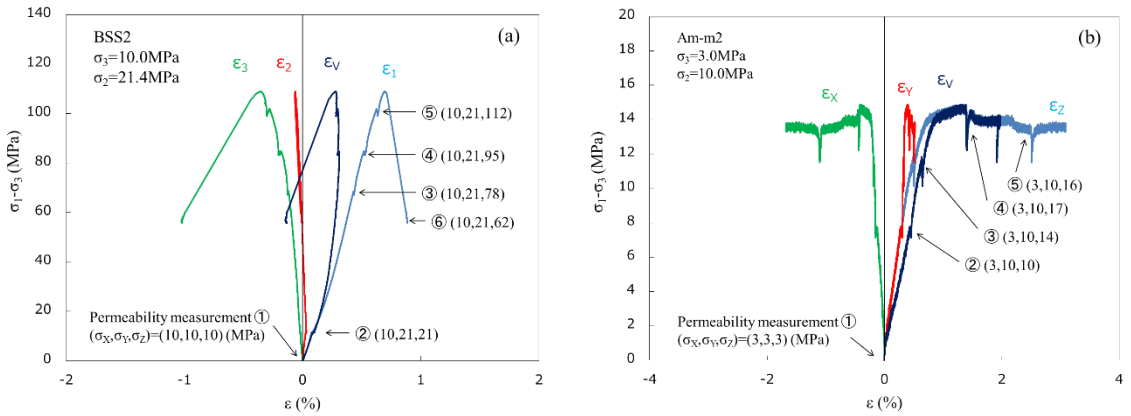

Fig. 4.4 The differential stress versus the strain for true triaxial experiment. Experimental conditions of (a) Berea sandstone (BSS2) was at a pore pressure of 1 MPa with confining pressures maintained 10MPa and σ2 maintained 21.4MPa, that of (b) Amatsu mudstone (Am-m2) was at a pore pressure of 1MPa with confining pressures maintained 3MPa and σ2 maintained 10MPa. The points of permeability tests are indicated by the arrows.

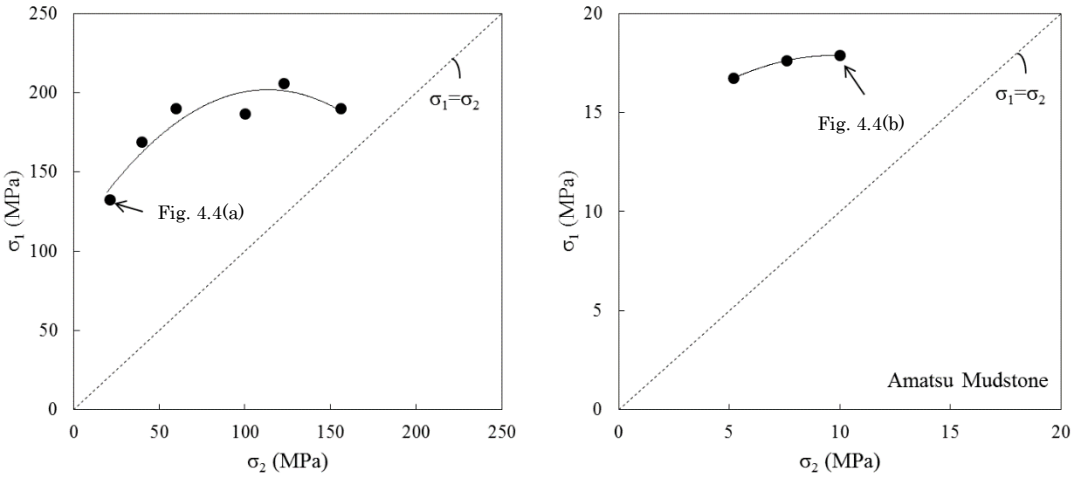

Fig. 4.5 True triaxial strength in tested (a) Berea sandstone and (b) Amatsu mudstone plotted as σ_1 at failure versus σ_2 for constant σ_3.

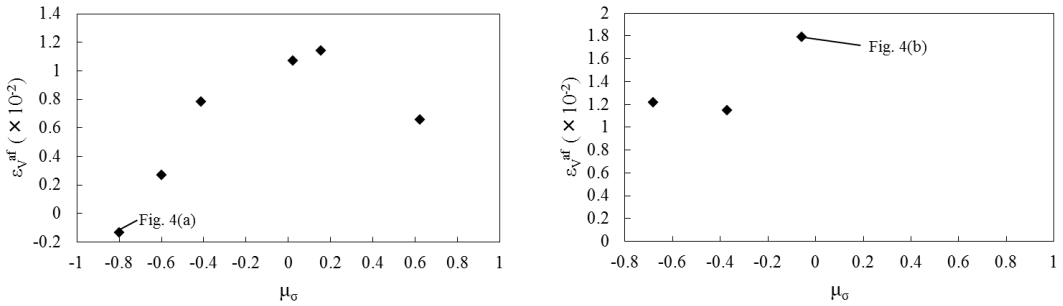

Fig. 4.6 Nadai–Lode parameter μ_σ versus volumetric strain after the peak stress ε_v^{pf}. The compressibility around $\mu_\sigma = 0$ is higher than for the other stress ratio.

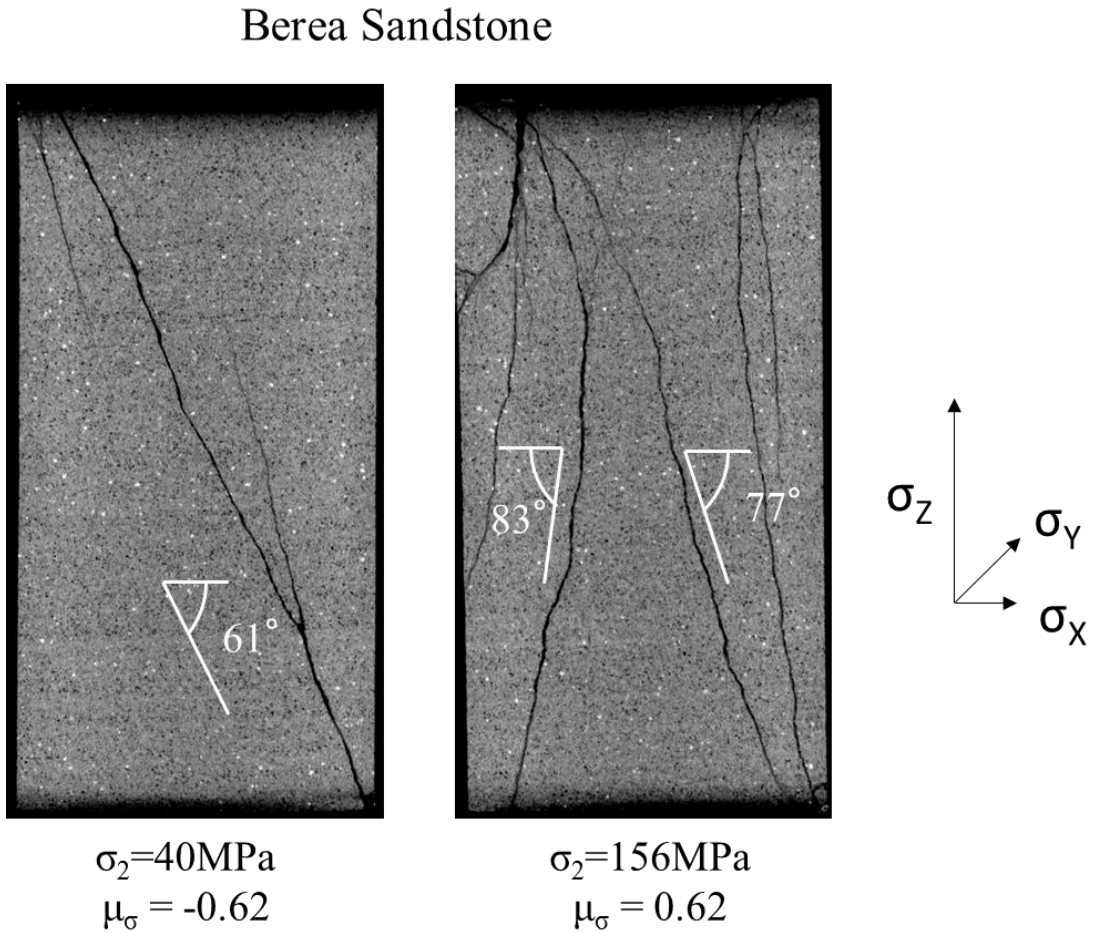

Fig. 4.7 micro-focus X-ray CT data of Berea sandstone after experiments under different σ_2 conditions.

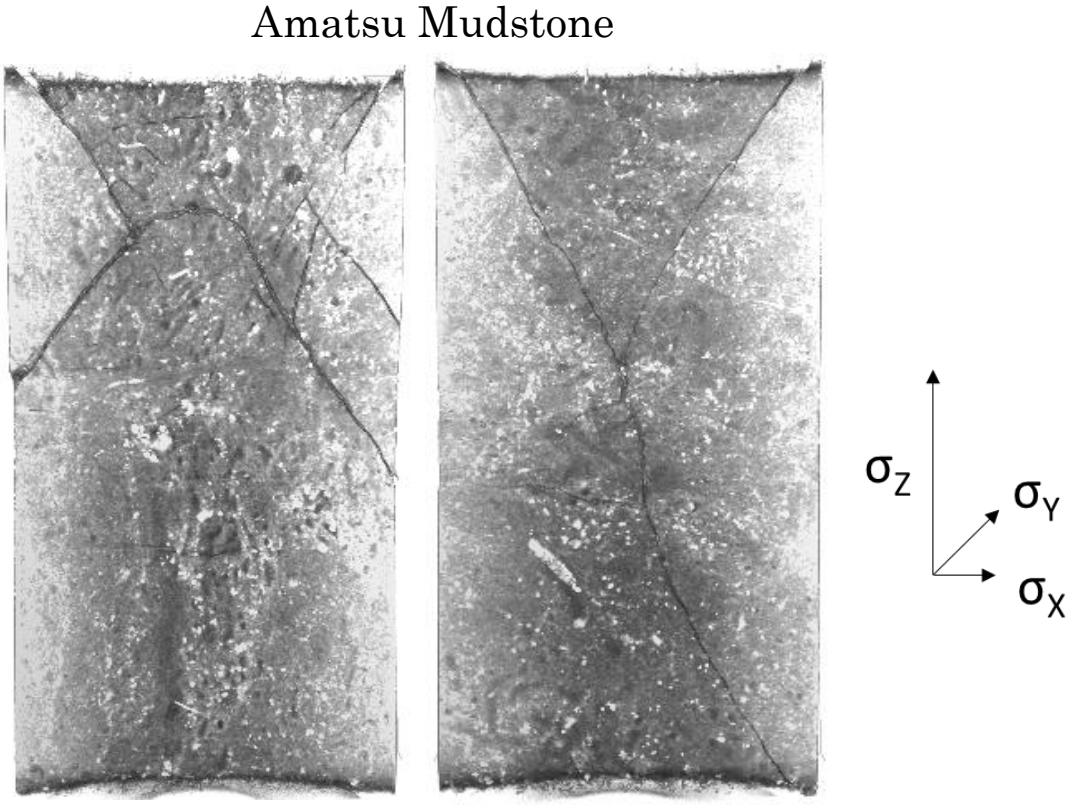

Fig. 4.8 Micro-focus X-ray CT data of Amatsu mudstone after experiments under different σ_2 conditions.

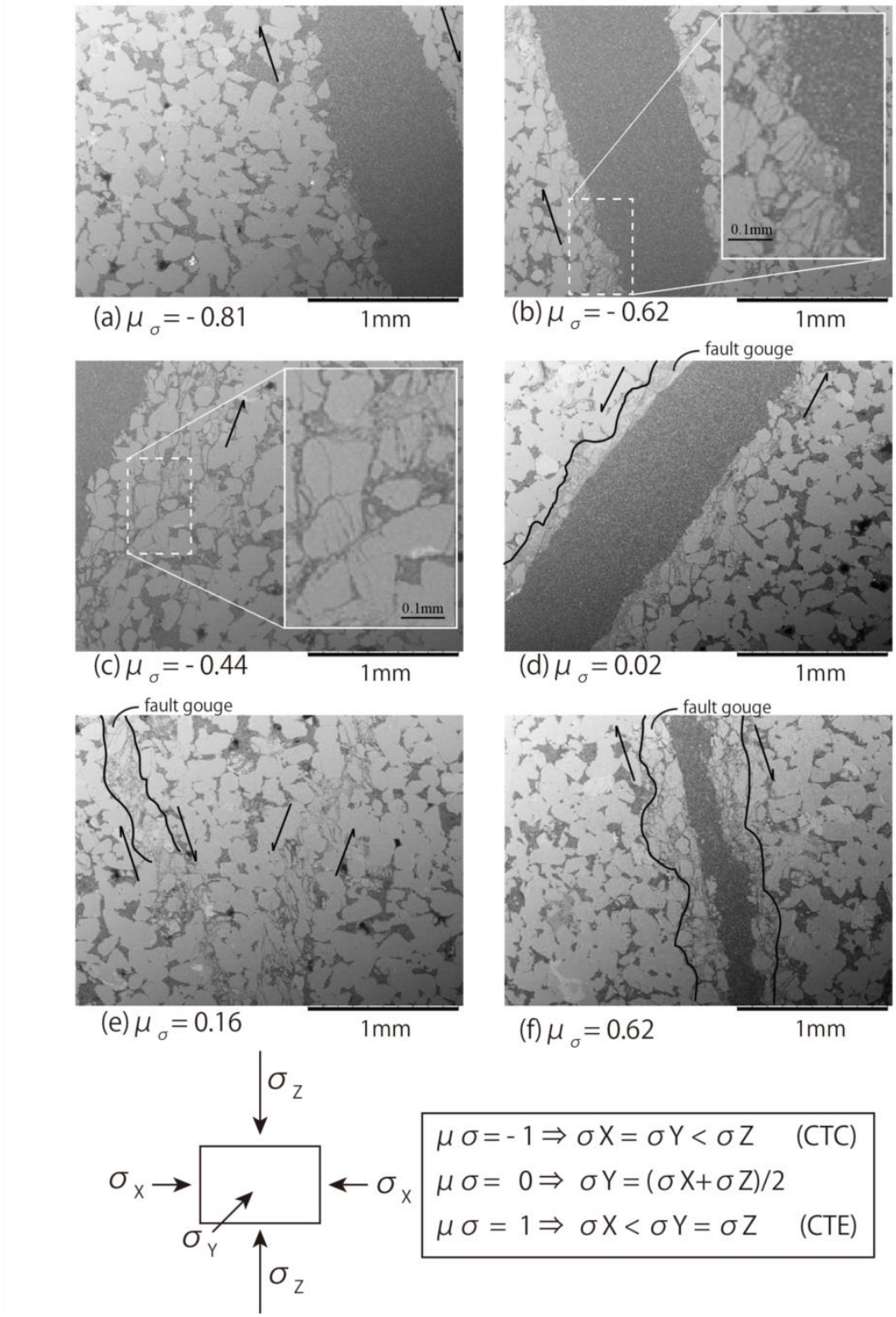

Fig. 4.9 Micrographs of the polished sections of Berea sandstone perpendicular to the Y direction after the experiment. The direction of shear movements are marked along the fault.

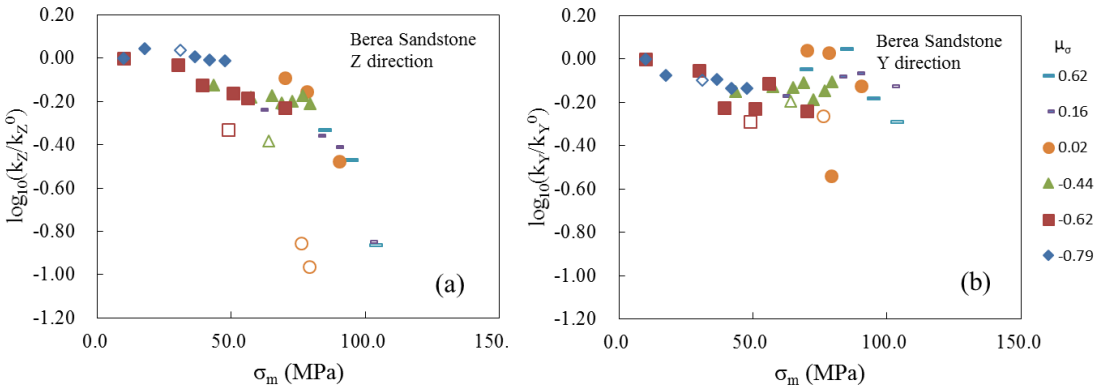

Fig. 4.10 Normalized permeability log10(k/k^0) versus mean stress σm for the Berea sandstone. The outlined symbols mean the point of the post-failure.

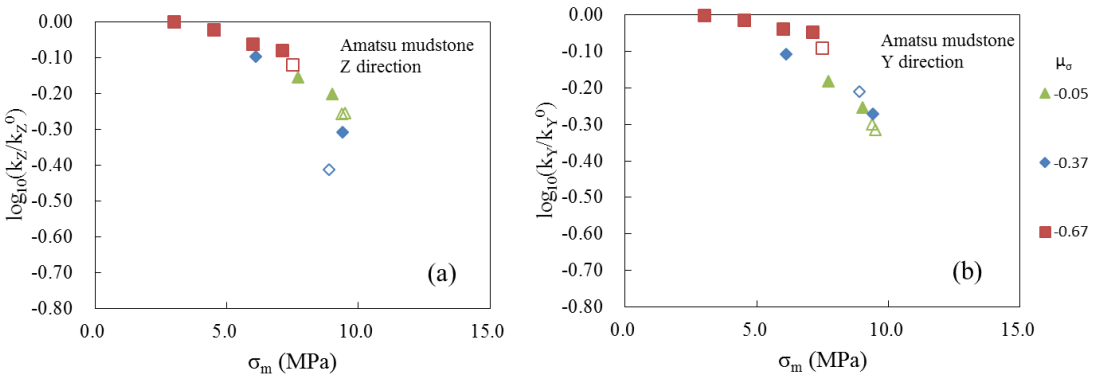

Fig. 4.11 Normalized permeability $\log_{10}(k/k^0)$ versus mean stress σ_m for the Amatsu mudstone. The outlined symbols mean the point of the post-failure.

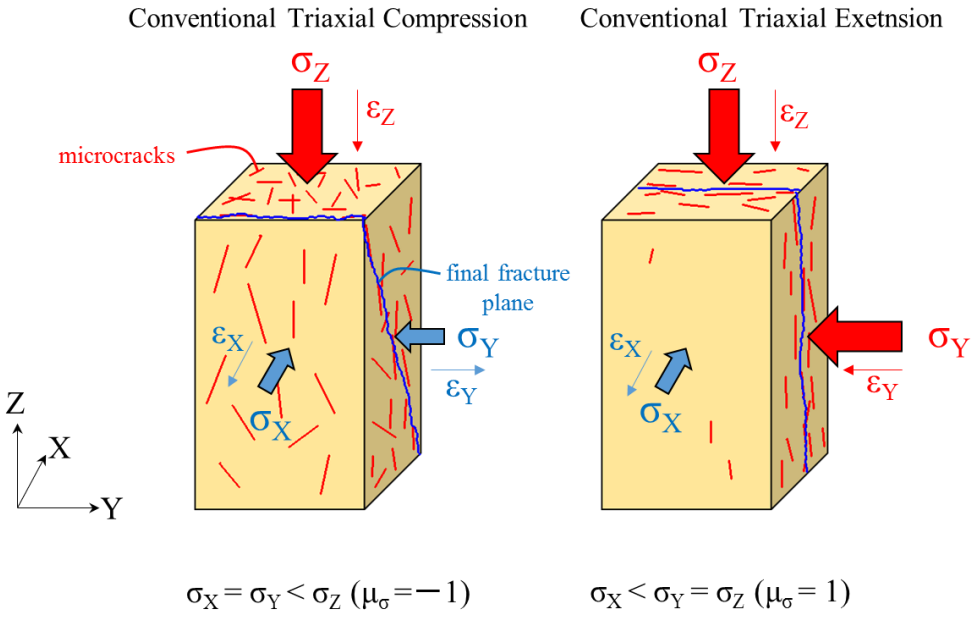

Fig. 4.12 Summary of crack distribution for $\mu_\sigma = -1$ (conventional triaxial compression) and $\mu_\sigma = 1$ (conventional triaxial extension) conditions under true triaxial stress. The thick arrows arrows mean loading stress. The thin arrows mean the directions of strain. The short red lines are cracks induced by loading. The blue lines are final fracture planes. The crack densities for stress induced microcracks, whose flat plane are perpendicular to the σ_X and σ_Y direction, were equal under $\mu_\sigma = -1$ condition. At higher σ_Y ($\mu_\sigma = 1$) condition, the crack density of the plane perpendicular σ_Y was reduced.

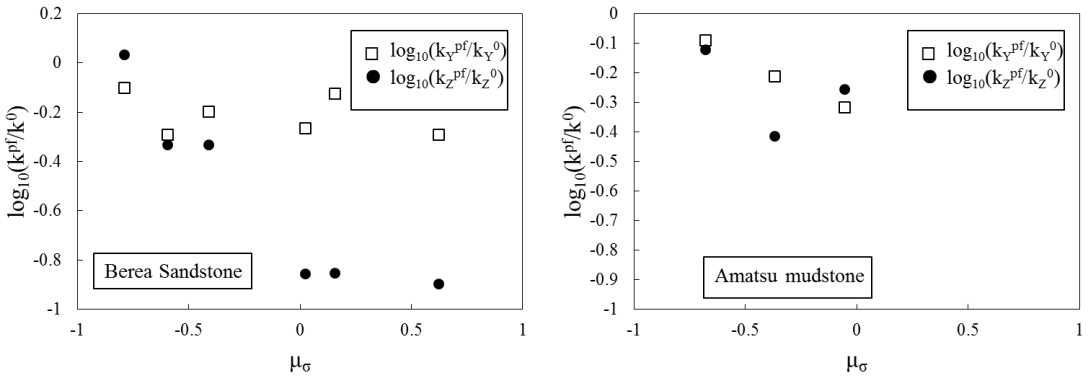

Fig. 4.13 Normalized permeability $\log_{10}(k^{pf}/k_0)$ versus stress ratio μ_σ for (a) Berea sandstone and (b) Amatsu mudstone.

Tab. 4.1 Experimental results

Sample number	Minimum stress	Intermediate stress	Maximum stress	Mean stress	Volume strain	Permeability of Y direction	Permeability of Z direction
(μ_σ at peak)	σ_3 (MPa)	σ_2 (MPa)	σ_1 (MPa)	σ_m (MPa)	ε_v (%)	k_Y ($\times 10^{-14} m^2$)	k_Z ($\times 10^{-14} m^2$)
BSS2	10.0	10.0	10.0	10.0	0.00	3.08	4.71
	10.0	21.4	21.4	17.6	0.10	2.58	5.21
	10.0	21.4	105.4	45.6	0.29	2.48	4.80
	10.0	21.4	114.9	48.8	0.30	2.25	4.64
	10.0	21.4	124.6	52.0	0.28	2.25	4.57
(-0.81)	10.0	21.4	132.6	54.7	0.28		
	10.0	21.4	62.3	31.2	-0.14	2.44	5.11
BSS5	10.0	10.0	10.0	10.0	0.00	7.92	11.30
	10.0	40.1	40.1	30.1	0.17	7.02	10.50
	10.0	40.1	67.9	39.3	0.32	4.70	8.46
	10.0	40.1	102.2	50.8	0.45	4.66	7.81
	10.0	40.1	118.1	56.1	0.50	6.13	7.41
	10.0	40.1	159.9	70.0	0.51	4.55	6.69
(-0.62)	10.0	40.0	169.0	73.0	0.53	0.00	0.00
	10.0	40.1	97.4	49.2	0.27	4.05	5.27
BSS3	10.0	10.0	10.0	10.0	0.00	7.66	16.60
	10.0	60.1	60.1	43.4	0.47	5.41	12.50
	10.0	60.1	101.8	57.3	0.57	5.72	11.00
	10.0	60.1	125.3	65.1	0.67	5.65	11.10
	10.0	60.1	136.6	68.9	0.72	5.97	10.30
	10.0	60.1	147.8	72.6	0.77	4.98	10.50
	10.0	60.1	160.0	76.7	0.82	5.45	11.10
	10.0	60.1	168.3	79.5	0.86	5.99	10.20
(-0.44)	10.0	60.0	189.8	86.6	0.93		
	10.0	60.1	122.6	64.2	0.79	4.87	6.86
BSS10	10.0	10.0	10.0	10.0	0.00	5.59	13.50
	10.0	100.0	100.0	70.0	0.92	6.12	11.00
	10.0	100.5	124.4	78.3	1.04	5.99	9.44
	10.0	100.5	160.8	90.4	1.27	4.20	4.50
(0.02)	10.0	100.4	186.6	99.0	1.24		
	10.0	100.5	118.4	76.3	1.07	3.04	1.88
	10.0	99.0	128.9	79.3	1.15	1.62	1.46
BSS7	10.0	10.0	10.0	10.0	0.00	5.16	12.50
	10.0	86.9	86.9	61.3	0.90	3.51	7.27
	10.0	118.9	118.9	82.6	1.08	4.29	5.48
	10.0	123.1	134.8	89.3	1.16	4.46	4.89
(0.16)	10.0	123.0	205.5	112.8	1.16		
	10.0	121.5	175.7	102.4	1.14	3.88	1.77
BSS8	10.0	10.0	10.0	10.0	0.00	4.14	7.52
	10.0	99.8	99.8	69.9	0.94	3.74	4.42
	10.0	116.8	128.2	85.0	1.23	4.62	3.53
	10.0	132.1	142.6	94.9	1.20	2.73	2.55
(0.62)	10.0	156.0	190.0	118.7	0.84		
	10.0	134.2	167.6	103.9	0.65	2.13	1.03

Tab. 4.1 Continued

Sample number	Minimum stress	Intermediate stress	Maximum stress	Mean stress	Volume strain	Permeability of Y direction	Permeability of Z direction
(μ_σ at peak)	σ_3 (MPa)	σ_2 (MPa)	σ_1 (MPa)	σ_m (MPa)	ε_v (%)	k_Y ($\times 10^{-17}m^2$)	k_Z ($\times 10^{-17}m^2$)
Am-m3	3.0	3.0	3.0	3.0	0.00	2.89	8.63
	3.0	5.2	5.2	4.5	0.25	2.81	8.21
	3.0	5.2	9.9	6.0	0.47	2.65	7.47
	3.0	5.3	13.0	7.1	0.68	2.60	7.20
(-0.67)	3.0	5.3	16.7	8.3	0.98		
	3.0	5.2	14.4	7.5	1.10	2.34	6.53
Am-m1	3.0	3.0	3.0	3.0	0.00	4.61	16.88
	3.0	7.6	7.6	6.1	0.28	3.61	13.50
(-0.37)	3.0	7.6	17.6	9.4	0.82	2.47	8.31
	3.0	7.6	16.1	8.9	1.38	2.84	6.50
Am-m2	3.0	3.0	3.0	3.0	0.00	5.08	9.22
	3.0	10.0	10.0	7.7	0.46	3.35	6.45
	3.0	10.0	14.0	9.0	0.64	2.83	5.78
(-0.05)	3.0	10.0	17.8	10.3	1.35		
	3.0	10.0	15.3	9.5	1.92	2.45	5.12
	3.0	10.0	15.1	9.4	1.92	2.54	5.08

Test pieces were fractured at stress conditions where peak μ_σ is described.

5. Application of permeability measurement under true triaxial stresses for modelling of accretionary prism

In this chapter, the experimental data of permeability under true triaxial stresses are compared with the *in-situ* data aiming to interpret the stress regime responsible for the development of accretionary complexes.

The field research into accretionary prisms and the proto-thrust zone suggests that *Calyptogena* or other chemosynthetic bio-communities form *en échelon* assemblages reflecting underlying fracture patterns. The fluids containing methane and/or other nutrients seep through these fractures and support the lives of the chemosynthetic bio-communities (Ogawa et al. 1996). Ogawa et al. (1996) proposed that the *en échelon* configuration implies a strike-slip stress regime with a vertical direction of σ_2. Ogawa and Asada (2009) proposed that this regime is common in deformation fronts. In the Berea sandstone of the current experiment, conjugate fractures were observed in the micrographs of specimens that were deformed under the $\mu_\sigma = 0.16$ condition (Fig. 4.9e). The permeability anisotropy $k_Y^{pf} > k_Z^{pf}$ was also favorable for high permeability in the σ_2 direction. This high permeability in the σ_2 direction is similar to the preferred fluid migration along the σ_2 direction (Ogawa et al. 1996), however, from the experimental viewpoint, high permeability in the σ_2 direction accompanied reducing permeability in the σ_1 direction during experiment at high μ_σ conditions.

In the Amatsu mudstone, the permeability anisotropy was not observed. The porosity of Amatsu mudstone was 40% based on mercury intrusion porosimetry and the porosity decreased with increasing mean stress (Fig. 4.6b). In the case of porous mediums such as mudstones, the permeability reduction with increasing stress is in common. Mondol et al. (2010) measured the vertical and horizontal permeability in a K_0-test (constant vertical stress under no lateral displacement of the specimen) using brine-saturated synthetic mudstones of varying textual and mineralogical compositions. They showed that the permeability

anisotropy produced by mechanical compaction in a K_0 condition was rather small compared with a function of clay mineralogy, grain size and the amount of silt in silt-clay mixtures.

In an accretionary prism, brittle or ductile deformation is induced by tectonic movement. If brittle deformation occurs, the permeability might be increased. However, the mudstone in the accretionary prism is too soft for brittle deformation to occur. Ishii et al. (2011) showed the brittle-ductile transition of mudstone using a brittleness index (BRI), which is the ratio of the unconfined compressive strength to the effective vertical stress. For mudstones under natural strain rates and low temperature, ductile deformation occurs when BRI < 2, brittle/ductile deformation occurs when BRI is 2–8, and brittle deformation occurs when BRI > 8 (Ishii et al. 2011). Kitajima et al. (2012) measured unconfined compressive strength of a core sample obtained from the Nankai accretionary prism. All of the mudstones and silty-mudstones that they studied were BRI < 2. The results for the Amatsu mudstone also illustrate ductile deformation (Fig. 4.4b) and permeability reduction increasing with increased mean stress (Fig. 4.11). In addition, the permeability anisotropy was not observed in Amatsu mudstone under all μ_σ conditions. The decreasing effective confining pressure results in increasing BRI and causes the brittle deformation. The effective confining pressure of this study was 2 MPa (confining pressure = 3 MPa, pore pressure = 1 MPa). In the Amatsu mudstone, the effective confining pressure decrease caused by excess pore pressure or decompression may lead to changes to the permeability property. The permeability of Amatsu mudstone is not to be increased under compressive stress under experimental conditions; however, the figure of micro focus X-ray CT after unloading (Fig. 4.8) shows fractures with a density lower than the surrounding rock mass. Therefore, it is probable that high permeability to σ_2 direction with stress release of the deformed rock after unloading. As for accretionary prism, fractures are opened by stress releasing induced by uplifting and/or erosion. Consequently, high permeability in the σ_2 direction of mudstone may also be observed in the surface of the seabed.

In a recent study by Chang et al. (2010), the *in-situ* stress tensor was measured using borehole breakouts in logging-while drilling (LWD) resistivity images of the borehole wall. This drilling induced borehole wall failures, which were either compressive (Bell and Gough, 1979), or tensile (Bell. 1996) fractures have been utilized to stress history. A recent Integrated Ocean Drilling Program (IODP) project, the Nankai Trough Seismogenic Zone Experiment, provides an opportunity to estimate *in-situ* stress states in the shallow Nankai accretionary prism. Several vertical boreholes were drilled in the shallow part of the accretionary prism (Fig. 5.1; Chang et al. 2010). The C0001 borehole penetrates the slope sediments to reach the accretionary prism. The C0002 borehole penetrates the sediments of the Kumano Forearc basin to reach the accretionary prism. The right-lateral strike-slip fault zone between boreholes C0001 and C0002 was drawn after Martin et al. (2010) analyzed the zone using 3-D seismic imaging. These images suggested that there is a significant tectonic decoupling in the form of strain partitioning across the strike-slip fault zone. Fig. 5.2 shows the ranges of maximum horizontal principal stress (S_{Hmax}) and minimum horizontal principal stress (S_{hmin}) normalized vertical overburden stress (S_v) at different depths described by Chang et al. (2010). In the upper part of borehole C0002, the areas enclosed by the normalized polygons lie mainly in the normal faulting stress regime. In the accretionary prism of borehole C0002, the ratio of S_{Hmax}/S_v increases, resulting in a probable strike-slip to a reverse faulting stress regime, depending on the S_{hmin} value. The upper part of borehole C0001 included slope sediment and the upper accretionary prism and the stress state is in favor of normal faulting. In the ruptured zone, the borehole pressure increased the over overburden; both horizontal stresses increase markedly above S_v, leading to a reverse faulting stress regime. In the lower accretionary prism of borehole C0001, the ratio of S_{Hmax}/S_v is larger than unity and S_{hmin}/S_v is smaller than unity, suggesting a strike-slip faulting regime. Fig. 5.3 shows the relationship between the intermediate principal stress ratio (μ_σ) and each of the fault regimes, as suggested by the true triaxial permeability test

described in Chapter 4. Here, to focus on fluid flow in the vertical direction, the three axes are rotated as follows: $\sigma_X = S_{hmin}$, $\sigma_Y = S_v$ and $\sigma_Z = S_{Hmax}$ (Fig. 5.3). The results of the true triaxial permeability test showed that in conditions of lower μ_σ, the permeability of post-failure specimens decreased compared with the initial permeability. In contrast, in the $\mu_\sigma > 0$ condition, the permeability of the σ_1 direction decreased more than the permeability of the σ_2 direction by forming a gouge layer parallel to σ_2 direction. The high permeability in the vertical direction is indicated with hatched lines in Fig. 5.3. Compared with the experimental data and *in-situ* data, the lower part of C0002 (Fig. 5.2) in the accretionary prism roughly conformed to the range of high permeability in the vertical direction. The lower accretionary prism in the C0001 borehole has a stress ratio of S_{Hmax}/S_v, which is slightly larger than the range of high permeability in the vertical direction. Another borehole, C0012 which is 25 km seaward site from C0006 (Fig. 5.1) penetrated from basin sediments to oceanic basement basalt (Yamamoto et al. 2013). Anelastic strain recovery measurements suggest a normal faulting regime in the basin sediments. In contrast, oceanic basement basalt shows a strike slip or reverse faulting stress regime with the maximum horizontal stress parallel to the plate convergence vector. The basement stress condition could be the result of hinge extension during bending of the Phillipine Sea plate, either in association with subduction or with the formation of an anticline during thrust (Yamamoto et al. 2013). In these ways, strike slip stress regime is unevenly distributed in marine sediments and rocks.

Besides, the results of permeability measurement under true triaxial test are applicable to normal fault and reverse fault rotating stress axes. Toki et al. (2004) inferred that the source of the seepage fluids in the Oomine Ridge in the Nankai accretionary prism, where several bacterial mats have been observed on the seafloor is horizontally transported groundwater. If the σ_2 oriented horizontal direction and deformed under high μ_σ condition, fluids may preferentially flow to horizontal direction. The experimental study for permeability change during deformation provides advantages for investigating the origin of the seeping fluids.

Afterward, Toki et al. (2014) investigated using Boron concentrations in the pore fluids suggested that the fluids are transported from depth via faults and are mixed with pore fluids in the shallow accretionary prism sediments and freshwater derived from methane hydrate dissociation prior to reaching the seafloor.

Measurements of *in-situ* stress and permeability have been significantly progressed and the results provide substantially important information regarding the stress states in submarine sediments. However, it remains very difficult to access the deep underground. Therefore, experimental study using the true triaxial permeability test has the potential to reinforce the *in-situ* data and develop an integrated model. However, there are problems associated with applying experimental data to *in-situ* data and/or modeling directly; for example, the size effect and the effect of the bedding plane. Therefore, it is necessary to expand experimental data using rocks which have different physical properties and run experiments to understand the influence of original anisotropy using test pieces with different directions to bedding plane. This thesis has described the experimental methods for measuring permeability anisotropy of sedimentary rocks during progressive deformation under true triaxial stress. Expanding permeability data under true triaxial test conditions will enhance the accuracy of the experimental data.

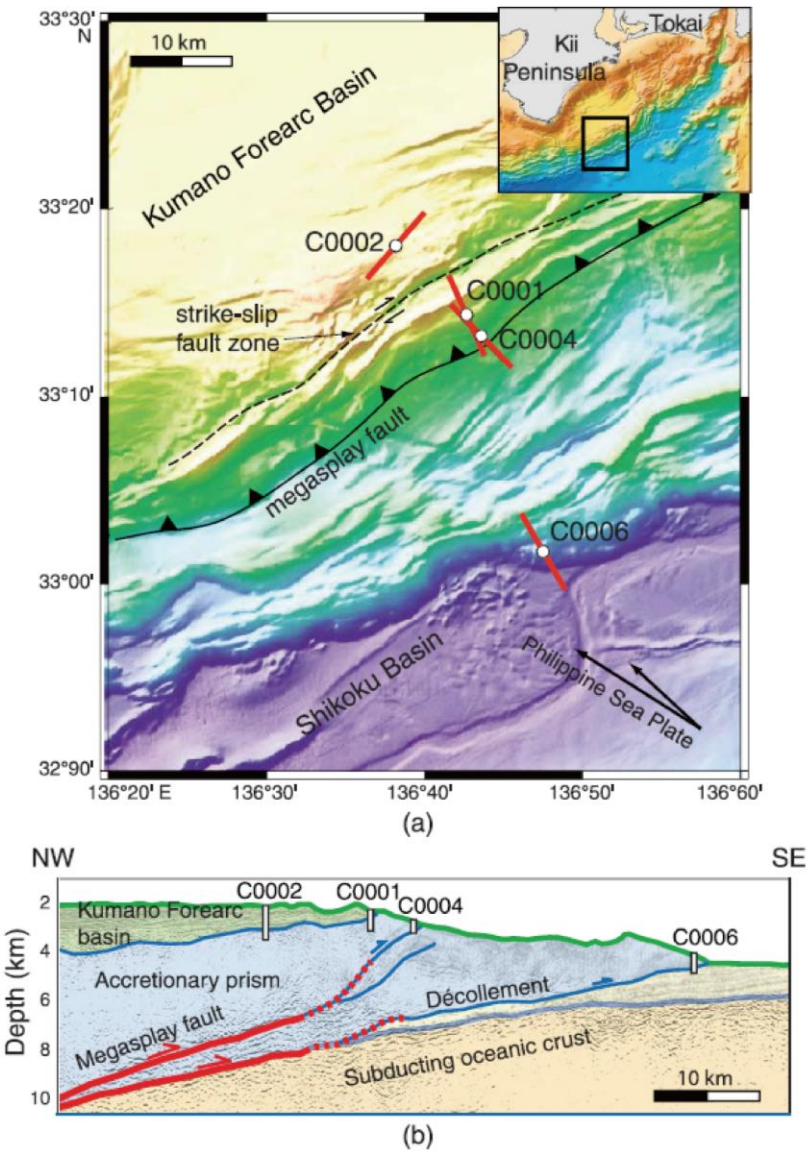

Fig. 5.1 (a) Borehole locations drilled in the shallow part of the accretionary prism in Nankai trough and (b) seismic reflection profile across the subduction zone and borehole locations (Chang et al. 2010).

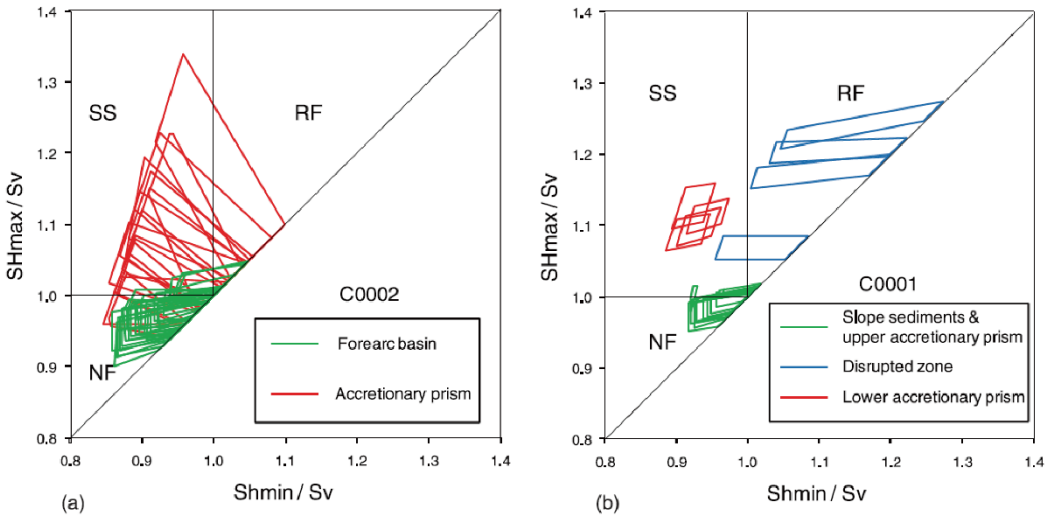

Fig. 5.2 The ranges of S_{Hmax} and S_{hmin} normalized S_v at different depths described by Chang et al. (2010). The stress regime varies in different structural domains. Borehole numbers are as shown in Fig. 5.1.

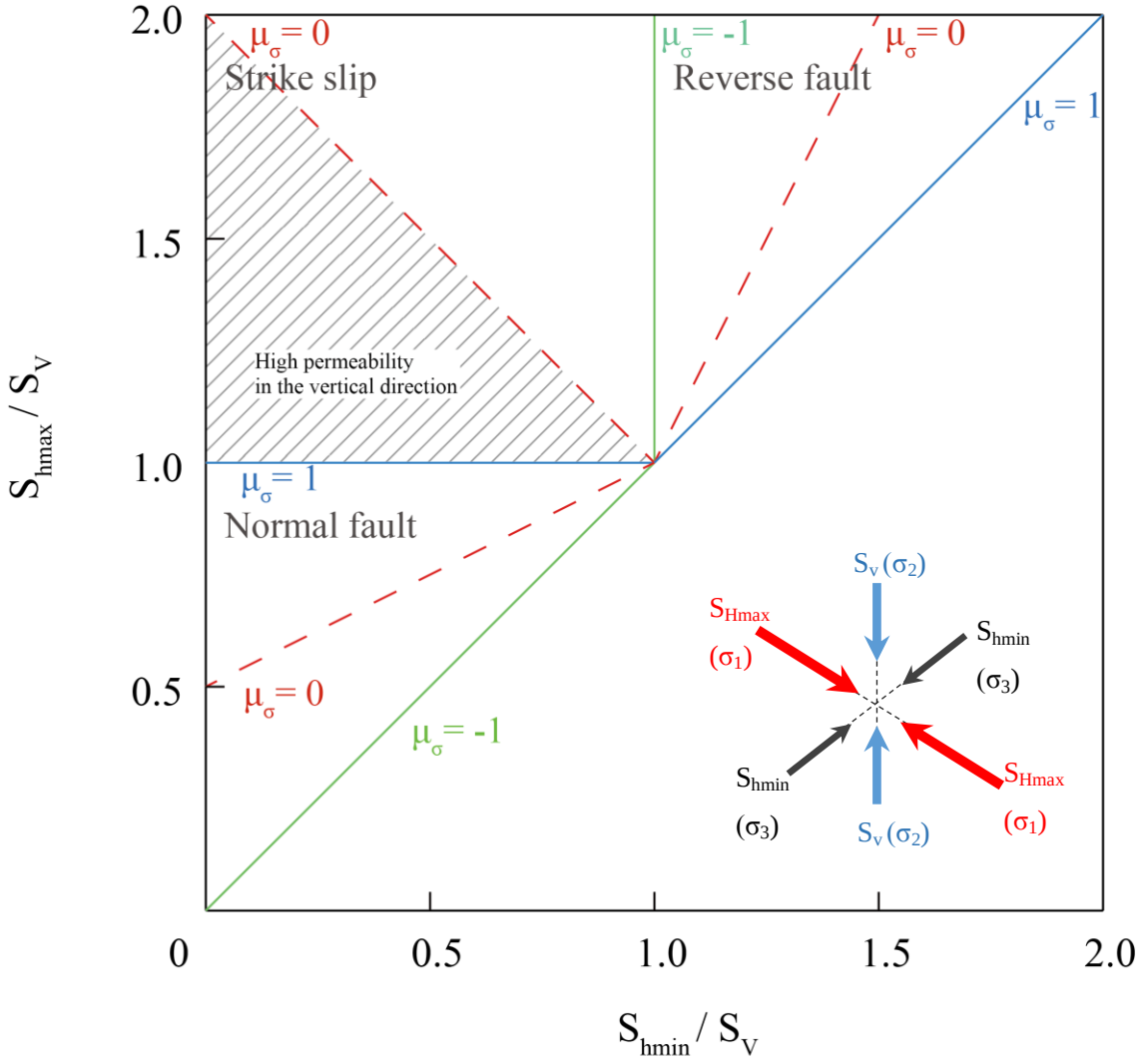

Fig. 5.3. Relationship of the intermediate principal stress ratio (μ_σ) and each fault regime suggested from true triaxial permeability test described in Chapter 4. The three axes are rotated from described in Chapter 4 as follows: $\sigma_X = S_{hmin}$, $\sigma_Y = S_v$ and $\sigma_Z = S_{Hmax}$. Green, blue and red lines denote $\mu_\sigma = -1$ (conventional confining), $\mu_\sigma = 0$ ($\sigma_2 = (\sigma_1 + \sigma_3)/2$) and $\mu_\sigma = 1$ (conventional extension) conditions, respectively.

6. Summary and Conclusions

Underground fluid migration needs to be examined in terms of permeability, and must also take faulting into account, because faulting can change the geological structure and permeability of the underground environment. The objective of this study is to evaluate the permeability change and permeability anisotropy for sedimentary rocks during deformation process under true triaxial stresses. The contents, results and conclusions of each chapter are as follows:

Chapter 1 described the previous study of laboratory permeability measurement of rocks and the objective of the present study. Stress dependence and shear deformation dependence of permeability were briefly reviewed. Previous studies using true triaxial test apparatus have revealed that σ_2 has the major control on fracture strength, mechanical behavior and crack distribution of rocks. It is clear that permeability is also dependent on the σ_2 value under constant σ_3 conditions; however, no previous study has measured the permeability of σ_1 and σ_2 directions simultaneously for sufficient repeatability under the above stress states. The objective of this study was to evaluate the permeability change and permeability anisotropy for sedimentary rocks under true triaxial stresses. Then, the necessity for obtaining deformation properties of submarine sedimentary rock which have a wide range of compressive strength and permeability properties was emphasized.

Chapter 2 observed physical and deformation of artificial specimens simulating submarine sedimentary rocks. Previous studies mainly suggested that the permeability properties during σ_1 loading were related to specimen strength and initial pore structures. Cataclasis and pore collapse cause decreasing permeability, and growth of microcracks causes increasing permeability under conventional triaxial tests. In this study, pore collapse with reorientation of sand particles, porosity reduction and tortuosity anisotropy were observed in the coherent shear band deformed specimen. The results mean the permeability reduction and permeability

anisotropy was occurred in the coherent shear band deformation specimen. However, permeability measurement was not able to conduct in this test. Then, it is necessary to measure the permeability of rocks during deformation.

Chapter 3 conducted permeability measurement to obtain hydraulic constants of rocks and considered the data acquisition method for obtaining fundamental hydraulic constants. Then, the experimental evaluation of hydraulic constants in mudstone using the flow pump method was indicated. Background information was then considered that sets the stage for the theoretical analysis for calculating hydraulic constants and evaluating error ranges based on the nonlinear-squares method. An improved experimental method introduced in this chapter was developed to obtain more accurate values of specific storage of specimens, considering the error range.

Chapter 4 presented the results of permeability measurements for Berea sandstone and Amatsu mudstone using Mogi-type true triaxial test apparatus. Results of permeability measurements on Berea sandstone suggested that σ_2 controls the mechanical behavior and crack distribution of deformed rocks under constant σ_3 conditions. The higher σ_2 condition induced the permeability anisotropy of Berea sandstones caused by fault gouge produced by cataclasis with brittle deformation. Results of Amatsu mudstone illustrated ductile deformation and permeability reduction with increasing mean stress. In addition, the permeability anisotropy was not observed in Amatsu mudstone of stress conditions. Therefore, mudstones have no permeability anisotropy resulted from deformation.

Chapter 5 compared experimental data of permeability under true triaxial stresses and *in-situ* data from previous studies. In an accretionary prism, brittle or ductile deformation is induced by tectonic movement. If brittle deformation occurs, permeability reduction and permeability anisotropy might be occurred accordingly depending on the stress states. However, the mudstone in accretionary prism is too soft to occur the brittle deformation. In the ductile deformation, the permeability reduction also might be occurred and no permeability

anisotropy resulted from deformation. Measurements of *in-situ* stress have been significantly progressed and the results provide substantial important information regarding the stress states in submarine sediments. However, it remains very difficult to access the deep underground. Therefore, experimental study using the true triaxial permeability test has the potential to reinforce the *in-situ* data and develop an integrated model.

This study contributes to understand deformation processes of sedimentary rocks in accretionary prisms for applications in structural geology. The experimental study for permeability change during deformation is also important for reservoir engineering such as evaluating water shielding structure for oil extraction, carbon capture and storage and high-level radioactive waste disposal. The results of this study progress laboratory permeability measurements and help to unravel complicated hydrologic deformation processes.

Acknowledgments

I would like to extend thanks to many people, who so generously contributed to the study presented in this thesis. I would like to express deepest appreciation to my supervisor, Dr. Ryo Anma, Graduate School of Life and Environmental Sciences, University of Tsukuba, for outstanding guidance, considerable encouragement and invaluable discussions during my work at the university. Similarly, special thanks go to Dr. Manabu Takahashi, Institute of Earthquake and Volcano Geology, National Institute of Advanced Industrial Science and Technology (AIST), for helping me with experiment techniques.

I am grateful to Dr. Takato Takemura, Nihon University, for his numerous and useful discussions. I am also hugely appreciative to Professor Yuichi Onda, and Dr. Teruyuki Maruoka, University of Tsukuba, for reading the earlier version of the manuscript and providing advice. I also thank Dr. Masaji Kato, Faculty of Engineering, Hokkaido University, for his suggestions in analytical solutions for the permeability test. I am deeply indebted to Drs. Daisuke Asahina and Takashi Fujii, AIST, for their discussions and encouragement. I also thank Mr. Kamran Panaghi, visiting scholar at Nihon University, who significantly improved the English manuscript.

References

Alam, A.K.M.B., Niioka, M., Fujii, Y., Fukuda, D., Kodama, J., 2014. Effects of confining pressure on permeability of three rock types under compression. Int. J. Rock Mech. Min. Sci. 65, 49‑61.

Atonellini, A., Aydin, A., 1994. Effect of faulting on fluid flow in porous sandstones; petrophysical properties. AAPG Bulletin. 78, 355-377.

Bell, J. S., 1996. In situ stresses in sedimentary rocks (part 1): Measurement techniques. Geoscience. Canada, 23, 85–100.

Bell, J. S., and Gough, D. I., 1979. Northeast-southwest compressive stress in Alberta: Evidence from oil wells. Earth Planet Science Letters. 45. 475-482.

Behrmann. J. H., 1991. Conditions for hydrofracture and the fluid permeability of accretionary wedges. Earth and Planetary Science Letters. 107. 550-558.

Brace, W. F., Walsh, J. B., Frangos, W. T., 1968. Permeability of granite under high pressure. Journal of Geophysical Research. Vol. 73, No, 6, pp.2225-2236.

Brace, W. F., 1980. Permeability of Crystalline and Argillaceous Rocks. International Journal of Rock Mechanics and Mining Sciences & Geomechanics Abstracts. Vol. 17, pp. 241-251.

Bruno, M. S., 1994. Micromechanics of stress-induced permeability anisotropy and damage in sedimentary rock. Mechanics of Materials. 18, 31-48.

Brown, G. O., 2002. Henry Darcy and the making of a law. Water resources Research, Vol. 38, No. 7, 1106, 10.1029/2011WR000727.

Byrne, T., Lin, W., Tsutsumi, A., Yamamoto, Y., Lewis, J., Kanagawa, K., Kitamura, Y.,Yamaguchi, A., Kimura, G., 2009. Anelastic strain recovery reveals extension acrossSW Japan subduction zone. Geophysical Research Letteers. Vol. 36, L23310, http://dx.doi.org/10.1029/2009GL040749

Chang, C., and Haimson, B., 2000. True triaxial strength and deformability of the German Continental Deep Drilling Program (KTB) deep hole amphibolite. J. Geophys. Res., 105, 18999-19013.

Chang, C., McNeill, L. C., Moore, J. C. Lin, W., Conin, M., Yamada, Y., 2010. In situ stress state in the Nankai accretionary wedge estimated from borehole wall failures. Geochemistry Geophysics Geosystems. Vol.11 http://dx.doi.org/10.1029/2010GC003261, Q0AD04.

Chen, L., Liu, J.F., Wang, C. P., Liu, J., Su, R., Wang, J., 2014. Characterization of damage evolution in granite under compressive stress condition and its effect on permeability. Int. J. Rock Mech. Min. Sci. 71. 340-349.

Dafalla, M., Shaker, A. A., Elkady, T., Al-Shamrani, M., Dhowian, A., 2015. Effects of confining pressure and effective stress on hydraulic conductivity of sand-clay mixtures. Arabian Journal of Geosciences. 8:9993-10001. DOI 10.1007/s12517-015-1925-1.

Dong, J-J., Hsu, J-Y., Wu, W-J., Shimamoto, T., Hung, J-H., Yeh, E. C., Wu, Y-H., and Sone, H., 2010. Stress-dependence of the permeability and porosity of sandstone and shale from TCDP Hole-A. International Journal of Rock Mechanics & Mining Sciences. Vol. 47, 1141-1157.

Esaki, T., Zhang, M., Takeshita, A., and Mitani. Y., 1996. Rigorous theoretical analysis of a flow pump permeability test. Geotechnical Testing Journal. Vol.19, pp. 241-246.

Evans, J. P., Forster, C. B., and Goddard, J. V., 1997. Permeability of fault-related rocks, and implications for hydraulic structure of fault zones. Journal of Structural Geology, Vol. 19, No. 11, pp. 1396-1404.

Farrell, N.J.C., Healy, D., Taylor, C.W., 2014. Anisotropy of permeability in faulted porous sandstones. J. Struct. Geol. 63. 50-67.

Faulkner, D. R., Jackson, C. A. L., Lunn, R. J., Schlische, R. W., Shipton, Z. K., Wibberley, C. A. J., 2010. A review of recent developments concerning the structure, mechanics and fluid

flow properties of fault zones. J. Struct. Geol. 32, 1557-1575.

Fujii, T., Uehara, S., and Sorai, M., 2015. Impact of effective pressure on threshold pressure of Kazusa Group mudstones for CO2 geological sequestration. Materials Transactions, Vol. 56, No. 4. pp. 519-528.

Hart, D. J., and Wang, H. F., 2001. A single test method for determination of poroelastic constants and flow parameters in rocks with low hydraulic conductivities. International Journal of Rock Mechanics & Sciences. Vol. 38, pp. 577-583.

Haimson, B., Chang, C., 2002. True triaxial strength of the KTB amphibolite under borehole wall conditions andits use to estimate the maximum horizontal in situ stress. J. Geophys. Res. 107, 2257-2271.

Haimson, B., and Rudnicki, J. W., 2010. The effect of the intermediate principal stress on fault formation and angle in siltstone. J. Struct. Geol. 32, 1701-1711.

Holtzman, R., and R. Juanes., 2011. Thermodynamic and hydrodynamic constraints on overpressure caused by hydrate dissociation: A pore-scale model. Geophy. Res. Letters 38.14.

Hsieh, P. A., Tracy, J. V. Neuzil, C. E., Bredehoeft, J. D., Silliman, S. E., 1981. A trasient laboratory method for determing the hydraulic properties of 'Tight' rocks-I. Theory. Int. J. Rock Mech. Min. Sci. & Geomech. Abstr. Vol. 18, pp. 245-252.

Ishii, E., Sanada, H., Funaki, H., Sugita, Y., 2011. The relationships among brittleness, deformation behavior, and transport properties in mudstones: An example from the Horonobe Underground Research Laboratory, Japan. J. Geophys. Res. 116, B09206.

Japan Atomic Energy Agency., 2003. Report. TJ5420 2004-004. pp.1-1 – 1-10.

Kameya, H., and Tokunaga, T., 2003. An Experimental study on the influence of the storage capacity of the experimental system on the flow pump hydraulic conductivity tests. Journal of MMIJ. Vol. 119, pp. 508-513.

Kato, M., Takahashi, M., and Kaneko, K., 2013. Highly Precise Evaluation of Hydraulic

Constants of Low-Permeability Rocks Using the Transient Pulse Method. Journal of MMIJ. Vol. 129, pp. 472-478.

Kawamura, T., Kato, M., Takahashi, M., and Kaneko, K., 2004. Proc. MMIJ Annual Meeting (2004), Vol. Ⅰ, pp. 89-90.

King, M. S., Chaudhry, N. A., and Shakeel, A., 1995. Experimental ultrasonic velocities and permeability for sandstones with aligned cracks. International Journal of Rock Mechanics and Mining Sciences & Geomechanics Abstracts. Vol. 32, pp. 155-163.

King, M. S., 2002. Elastic wave propagation in and permeability for rocks with multiple parallel fractures. Int. J. Rock Mech. Min. Sci. & Geomech. Abstr. 39, 1033-1043.

Kitajima, H., Chester, F. M., Biscontin, G., 2012. Mechanical and hydraulic properties of Nankai accretionary prism sediments: Effect of stress path. Geochem. Geophys. Geosyst. 13, Q0AD27, doi: 10. 1029/2012GC004124.

Kobayashi. K., 2002. Tectonic significance of the cold seepage zones in the eastern Nankai accretionary wedge - an outcome of the 15 years' KAIKO projects. Marine Geology. 187, 3-30.

Kwon, O., Kronenberg, A. K., Gangi, A. F., Johnson, B., and Herbert, B. E., 2004. Permeability of illite-bearing shale: 1. Anisotropy and effects of clay content and loading. Journal of Geophysical research. Vol. 109, B10205, doi:10.1029/2004JB003052.

Li. X., Wu. Zhishen., Takahashi. M., Yasuhara. K., 2002. Permeability anisotropy of shirahama sandstone under true triaxial stresses. J. Geotech, JSCE, 708/Ⅲ-59, 1-11.

Lin, W., 1977. Compressible fluid flow through rocks of variable permeability, Lawrence Livermore Laboratory, Livermore, California, Rept. UCRL-52304.

Lin, W., Takahashi, M., Hirono, T., and Sasaki, T., 2003. A brief review on comparison of permeabilities by various measurement techniques in laboratory. Journal of MMIJ. Vol. 119, pp. 519-522.

Lin, W., Byrne, T. B., Kinoshita, M., McNeill, L. C. Chang, C., Lewis, J. C., Yamamoto, Y.,

Saffer, D. M., Moore, J. C., Wu, H.-Y., Tsuji, T., Yamada, Y., Conin, M., Saito, S., Ito, T., Tobin, H. J., Kimura, G., Kanagawa, K., Ashi, J., Underwood, M. B., Kanamatsu, T., 2015. Distribution of stress state in the Nankai subduction zone, southwest Japan and a comparison with Japan Trench. Techtonophysics. doi:10.1016/j.tecto.2015.05.008. In print.

Martin, K.M., Gulick, S.P.S., Bangs, N.L.B.,Moore, G.F., Ashi, J., Park, J.-O., Kuramoto, S., Taira, A., 2010. Possible strain partitioning structure between the Kumano fore‐arc basin and the slope of the Nankai Trough accretionary prism. Geochemistry Geophysics Geosystems. Vol.11, Q0AD02. http://dx.doi.org/10.1029/2009GC002668.

Menéndez, B., Zhu, W., Wong, T.-F., 1996. Micromechanics of brittle faulting and cataclastic flow in Berea sandstone. J. Struct. Geol. 18, 1-16.

Meng, Z., and Li, G., 2013. Experimental research on the permeability of high-rank coal under a varying stress and its influencing factors. Engineering Geology, Vol. 162, pp. 108-117.

Mitchell, T. M., Faulkner, D. R., 2008. Experimental measurements of permeability evolution during triaxial compression of initially intact crystalline rocks and implications for fluid flow in fault zones. J. Geophys. Res. 113, B11412.

Miller, A. W. and Wang, Y., 2012. Radionuclide Interaction with Clays in Dilute and Heavily Compacted Systems: A Critical Review. Journal of Environmental Science & Technology, Vol. **46**, pp. 1981-1994.

Mogi, K., 1971a. Fracture and flow of rocks under high triaxial compression, J. Geophys. Res. 76, 1255-1269.

Mogi, K., 1971b. Effect of triaxial stress systems on the failure of dolomite and limestone. Tectonophysics.11, 111-127.

Mondol, N. H., Jahren, J., Berre, Toralv., Grande, L., Bjørlykke., 2010. AAPG Annual Convention and Exhibition. Search and Discovery Article. #40649.

Morin, R. H., and Olsen. H. W., 1987. Theoretical analysis of the transient pressure response

from a constant flow rate hydraulic conductivity test. Water Resources Research, Vol.23, pp. 1461-1470.

Nasseri, M. H. B., Goodfellow, S. D., Lombos, L., Young, R. P., 2014. 3-D transport and acoustic properties of Fontainebleau sandstone during true-triaxial deformation experiments. International Journal of Rock Mechanics and Mining Sciences. Vol. 69, pp. 1-18.

Neuzil, C. E., Cooley, C., Siliman, S. E., Bredehoeft, J. D., and Hsieh, P. A., 1981. A transient laboratory method for determining the hydraulic properties of 'tight' rocks—I. Theory. International Journal of Rock Mechanics and Mining Sciences & Geomechanics Abstracts. Vo.18, pp. 253-258.

Nishio, S., Ogisako, E., and Denda, T., 2003. Seabed deformation during methane hydrate production –Part1: Engineering properties of Nankai trough sediments. Proceedings of annual conference of Japanese Geotechnical Society, 38. pp. 375-376.

O'Connel, R. J., and Budiansky, B., 1974. Seismic velocities in dry and saturated cracked solids. J. Geophys. Res. 79, 6667-6674.

Ogawa, Y., Fujioka, K., Fujikura, K., and Iwabuchi, Y., 1996. *En échelon* patterns of *Calyptogena* colonies in the Japan Trench. Geology. 24, 807-810.

Ogawa, Y., and Vrolijk, P., 2006. Control of internal structure and fluid-migration pathways within the Barbados Ridge decollement zone by strike-slip faulting: Evidence from coherence and three-dimensional seismic amplitude imaging. Discussion. Geol. Soc. America. Bull, 118, 253-254, doi: 10.1130/B25513.1

Ogawa, Y., and Asada, M., 2009. Tectonic implications of strike-slip fault regime at the leading edge of an accretionary prism. Earth Evolution Sciences. 3, 27-36.

Oku, H., Haimson, B., Song, S-R., 2007. True triaxial strength and deformability of the siltstone overlying the Chelungpu fault (Chi-Chi earthquake), Taiwan. Geophys. Res. Lett. 34, L09306.

Olsen, H. W., 1966. Darcy's law in saturated kaolinite. Water Resour. Res. 2, 287-295.

Sato, M., Takahashi, M., Takemura, T., 2013. Experimental studies on deformability and permeability of artificial unconsolidated to partially consolidated sediments. Jour. Japan Soc. Eng. Geol., Vol. 54, No. 4, pp. 168-174.

Sato, M., Kato, M., Takahashi, M., 2016. Experimental evaluation of specific storage in mudstone considering error using the flow pump method. Materials Transactions. Vol. 57, No. 2, pp. 112-118.

Shipton, Z. K., Evans, J. P., Robeson, K. R., Forsster, C. B., Snelgrove, S., 2002. Structural heterogeneity and permeability in faulted eolian sandstone: implications for subsurface modeling of faults. AAPG Bulletin. 86(5), 863-883.

Shipton, Z. K., Evans, J. P., Thompson, L. B., 2005. The geometry and thickness of deformation band fault core, and its influence on sealing characteristics of deformation band fault zones. American Association of Petroleum Geologists Memoir 85, 181-195.

Sibson, R. H., Moore, J. M., Rankin, A. H., 1975. Seismic pumping－a hydrothermal fluid transport mechanism. Journal of Geological Society, Vol. 131, No. 6, pp. 653-659.

Soga, N., Mizutani, H., Spetzler, H., Martin, R. J. III., 1978. The effect of dilatancy on velocity anisotropy in Westerly granite. J. Geophys. Res. 83, 4451-4458.

Song, I., Elphic, S. C., Main, I. G., Ngwenya, B. T., Odling, N. W., and Smyth, N. F., 2004. One-dimensional fluid diffusion induced by constant-rate flow injection: Theoretical analysis and application to the determination of fluid permeability and specific storage of a cored rock sample. Journal of Geophysical Research. vol. 109, B05207, doi:10.1029/2003JB002395.

Song, J. and Zhang, D., 2013. Comprehensive Review of Caprock-Sealing Mechanisms for Geologic Carbon Sequestration. Journal of Environmental Science & Technology, Vol. **47**, pp. 9-22.

Takahashi, M., Hirata, A., and Koide, H., 1990. Effect of Confining pressure and pore

pressure on permeability of Inada Granite. Journal of the Japan Society of Engineering Geology. Vol.31. No. 3. pp.1-10.

Takahashi, M., Sugita, Y., and Xue, Z., 1993. Three principal stress effects on permeability of Shirahama sandstone – In case of stress state prior to dilatancy, J. The Mining and Materials Processing Institute of Japan, Vol. 109, pp. 803-808.

Takahashi, M., Li, X., Lin, W., Narita, T., Tomishima, Y., 2004. Characteristics of hydraulic conductivity along the final fault plane under true triaxial stress. Proc. Int. Symp. Int. Soc. Rock Mech. Regional symposium, Europian Rock 2004 and 53rd Geomechanics Colloquium, 507-510.

Takahashi, T.,Takahashi, M., Kiyama, T., Takemura, T., 2009. A triaxial compression and triaxial extension test of Kimachi sandstone. Proceedings of the EUROCK2009. 381-386.

Takahashi, M., 2012. Seismic wave velocity anisotropy in Westerly granite under a true triaxial compression test, True Triaxial Testing of Rocks, Geomechanichs Research Series. CRC Press. 4, 193-202.

Takahashi, M., Park, H., Fujii, M., Sato, M., 2014. Deformation behavior and shear wave velocity under confined triaxial extension stress. Rock Eng. and Rock Mech. Structures in and on Rock Masses. 179-182.

Tanikawa, W., Shimamoto, T., Wey, S.-K., Lin, C.-W., and Lai, W,-C., 2008. Stratigraphic variation of transport properties and overpressure development in the Western Foothills, Taiwan. Journal of Geophysical Research. Vol. 113, B12403, doi:10.1029/2008JB005647.

Toki, T., Higa, R., Ijiri, A., Tsunogai, U., Ashi, J., 2014. Origin and transport of pore fluids in the Nankai accretionary prism inferred from chemical and isotopic compositions of pore water at cold seep sites off Kumano. Earth, Planets and Space, 66.137, doi:10.1186/s40623-014-0137-3.

Toki T, Tsunogai U, Gamo T, Kuramoto S, Ashi J (2004) Detection of low-chloride fluids beneath a cold seep field on the Nankai accretionary wedge off Kumano, south of Japan.

Earth Planet Sci Lett 228:37–47.

Tokunaga, T., Aoyagi, R., Mogi, K., Kameya, H., and Tosaka, H., 2001. Determination of hydraulic conductivity and storage coefficient through simultaneous measurements of fluid pressure and strains. Journal of the Japan Society of Engineering Geology. Vol.42, pp. 208-213.

Tokunaga, T., and Kameya, H., 2003. Determination of specific storage of a porous material from flow pump experiments: theoretical analysis and experimental evaluation. International Journal of Rock Mechanics & Mining Sciences. Vol.40, pp. 739-745.

Uehara, S., Shimamoto, T., Okazaki, K., Funaki, H., Kurikami, H., Niizato, T., and Ohnishi, Y., (2012) Can surface samples be used to infer underground permeability structure? A test case for a Neogene sedimentary basin in Horonobe, Japan. International Journal of Rock Mechanics & Mining Sciences, Vol. 56 , pp. 1-14.

Uehara, S., and Takahashi, M., 2014. Evolution of permeability and microstructure of experimentary-created shear zones in Neogene siliceous mudstones from Horonobe, Japan. J. Struct. Geol. 60, 46-54.

Walsh, J. B., 1981. Effective of pore pressure and confining pressure on fracture permeability. International Journal of Rock Mechanics and Mining Sciences & Geomechanics Abstracts. Vol. 18, pp. 429-435.

Wibberley, C.A.J., 2002. Hydraulic diffusivity of fault gouge zones and implications for thermal pressurization during seismic slip. Earth Planets Space, 54, 1153-1171.

Wibberley, C. A. J., and Shimamoto, T., 2003. Internal structure and permeability of major strike-slip fault zones: the Median Tectonic Line in Mie Prefecture, southwest Japan. Journal of Structural Geology. Vol. 25, pp. 59-78.

Wong, T. F., and Baud, P., 1999. Mechanical compaction of porous sandstone. Oil & Gas Science and Technology. Vol. 54, No. 6, pp. 715-727.

Yamamoto, Y., Lin, W., Oda, H., Byrne, T., Yamamoto, Y., 2013. Stress states at the

subduction input site, Nankai Subduction Zone, using anelastic strain recovery (ASR) data in the basement basalt and overlying sediments. Tectonophysics. 600. 91-98.

Zeng, Z., Li, X., Shi, L., Bai, B., Fang, Z., Wang, Y., 2014. Experimental study of the laws between the effective confining pressure and mudstone permeability. Energy Procedia. Vol. 63, pp. 5654-5663.

Zhang, M., Takahashi, M., Morin, R. H. and Esaki, T., 2000. Evaluation and application of the transient-pulse technique for determining the hydraulic properties of low-permeability rocks -- Part 1: Theoretical evaluation. Geotechnical Testing Journal. Vol. 23, pp. 91-99.

Zhang, S., Tullis, T E., 1998. The effect of fault slip on permeability and permeability anisotropy in an artificial quartz gouge. Tectonophysics. 295, 41-52.

Zhang, M., Takahashi, M., Morin, R. H., Endo, H., Esaki, T., 2002. Determining the hydraulic properties of saturated, low-permeability geological materials in the laboratory: Advances in theory and practice. Evaluation and Remediation of low permeability and dual porosity environments, ASTM STP 1415, ASTM International, West Conshohocken. 83-98.

Zhu, W., Montesi, L. G. J., Wong, T., 1997. Shear-enhanced compaction and permeability reduction: Triaxial extension tests on porous sandstone. Mechanics of Materials. 25, 199-214.

Zhu, W., Montesi, L. G. J., and Wong, T. -F., 2002. Effects of stress on the anisotropic development of permeability during mechanical compaction of porous sandstones. Geol. Soc. London, Special Publications. 200, 119-136.

Zoback, M. D., Byerlee, J. D., 1976. Effect of high pressure deformation on permeability of Ottawa Sand. AAPG. Bull. 60, 1531-1542